JOURNAL OF GEOPHYSICAL RESEARCH, VOL. 99, NO. D9, PAGES 18,585–18,604, SEPTEMBER 20, 1994

# Observations of the Earth's Radiation Budget in relation to atmospheric hydrology 4. Atmospheric column radiative cooling over the world's oceans

Graeme L. Stephens,[1] Anthony Slingo,[2] Mark J. Webb,[2] Peter J. Minnett,[3] Peter H. Daum,[3] Lawrence Kleinman,[3] Ian Wittmeyer,[1] and David A. Randall[1]

**Abstract.** This paper introduces a simple method for deriving climatological values of the longwave flux emitted from the clear sky atmosphere to the ice-free ocean surface. Simulations of the clear sky longwave fluxes to space and to the surface are employed in this study to assist in the development of this flux retrieval which requires monthly averaged column-integrated water vapor $w$ and the clear sky top–of–atmosphere (TOA) outgoing longwave flux (both available from satellite measurements). It is shown using both theory and data from simulations how the ratio of the surface to TOA flux is a simple function of $w$ and a validation of the simple relationship is presented based on a limited set of surface flux measurements. The rms difference between the retrieved surface fluxes and the simulated surface fluxes is approximately 6 W $m^{-2}$. The clear sky column cooling rate of the atmosphere is derived from the Earth Radiation Budget Experiment (ERBE) values of the clear sky TOA flux and the surface flux retrieved using Special Scanning Microwave Imager (SSM/I) measurements of $w$ together with ERBE clear sky fluxes. The relationship between this column cooling rate, $w$, and the sea surface temperature (SST) is explored and it is shown how the cooling rate systematically increases as both $w$ and SST increase. The uncertainty implied in these estimates of cooling are approximately $\pm 0.2$ K $d^{-1}$. The effects of clouds on this longwave cooling are also explored in a limited way by placing bounds on the possible impact of clouds on the column cooling rate based on certain assumptions about the effect of clouds on the longwave flux to the surface. While a more global assessment of the cloud effect must await use of new satellite data that will allow us to estimate the contributions by clouds to these surface fluxes, it is shown in this paper how the longwave effects of clouds in a moist atmosphere where the column water vapor exceeds approximately 30 kg $m^{-2}$ may be estimated from presently available satellite data with an uncertainty estimated to be approximately 0.2 K $d^{-1}$. Based on an approach described in this paper, we show how clouds in these relatively moist regions decrease the column cooling by almost 50% of the clear sky values and the existence of significant longitudinal gradients in column radiative heating across the equatorial and subtropical Pacific Ocean.

## 1. Introduction

The energy balance of the Earth, the distribution of energy in space, and its variation in time are fundamental characteristics of the Earth's climate system. It is crucial to understand how this energy balance is altered in response to increased concentrations of greenhouse gases to understand and ultimately predict any impending global climate change. Unfortunately, quantitative estimates of the individual components of this energy budget, even in its most rudimentary annual and global–mean form, are subject to large uncertainties since many of the key fluxes of energy are yet to be measured over the globe. For instance, the fluxes of energy to and from the surface, at least on the global scale, are primarily derived from model calculations or estimated from empirical formulae and must be considered highly uncertain [e.g.,*Randall et al.*, 1992; *Gupta et al.*, 1992]. Methods using satellite observations for retrieving these fluxes, with the exception of the solar flux to the surface

[1]Department of Atmospheric Science, Colorado State University, Ft. Collins, Colorado.

[2]Hadley Center for Climate Prediction and Research, Bracknell, England.

[3]Brookhaven National Laboratory, Upton, New York.



Paper number 94JD01151.
0148-0227/94/94JD-01151$05.00

[e.g., *Schmetz*, 1989; *Pinker and Laszlo*, 1992; *Cess et al.*, 1991], remain largely undeveloped. Despite this situation, important but limited advances to our view of this global energy balance have emerged from satellite measurements of the radiative fluxes at the top of the atmosphere. These advances began in the late 1960s and continue into the present through the Earth Radiation Budget Experiment (ERBE), [*House et al.*, 1986].

This paper is the final in a series [*Stephens and Greenwald*, 1991a,b, hereafter referred to as parts 1 and 2; *Stephens et al.*, 1993, hereafter part 3], which seek to explore new uses of global satellite data to study relationships between certain components of the energy budget and the hydrological cycle of the climate system. The motivation, in part, is to develop useful diagnostic tests of current global climate models and, in part, to study rudimentary relationships between radiation and the atmospheric branch of the Earth's hydrological cycle. The main aim of this paper is to introduce a simple method for deriving climatological values of the longwave flux emitted from the clear sky atmosphere to the surface (hereafter denoted as $F_g$) and in so doing explore the connection between the longwave radiation budget and the water vapor content of the atmosphere. The flux $F_g$ is one of the principal drivers of the planet's greenhouse effect. It is the emission of infrared radiation from the atmosphere to the surface that maintains the mean surface temperature of the Earth (approximately 288 K) above the mean effective temperature of the planet (approximately 255 K). It is also the amplification of this flux due to increased concentrations of water vapor, driven by increased concentrations of other greenhouse gases, that is thought to establish the water vapor feedback [*Manabe and Wetherald*, 1967].

We currently estimate that the globally averaged atmosphere constantly loses energy by radiation at a rate of approximately 100 W $m^{-2}$ [*Ramanathan et al.*, 1989]. It is a related goal of this study to estimate the clear sky longwave contribution to this loss as well as the longwave contributions by clouds in selected regions of the globe. The loss of radiative energy by the atmosphere is compensated by energy transfer from the surface via convective and turbulent transfer processes. The global balance achieved in the atmosphere through the combination of the radiative and nonradiative processes is generally referred to as a radiative–convective equilibrium. The major contributors to this equilibrium is the flux of heat supplied by latent heating, associated with precipitation in the atmosphere, and the loss of longwave radiant energy by the atmosphere. It is common to express this loss of radiant energy as the rate of cooling of the atmospheric column. Global scale changes in this cooling imply compensating changes in latent heating and thus changes in the Earth's hydrological cycle. It is appropriate then to consider this cooling as a fundamental measure of the activity of the Earth's greenhouse effect and in turn an indirect measure of the activity of the hydrological cycle in heating the atmosphere.

Section 2 offers a brief account of the data used in the present study, and section 3 introduces results from the simulation system of *Slingo and Webb* [1992], which are subsequently used in section 4 to develop a new diagnostic method for the retrieval from satellite data of $F_g$. Results of this retrieval approach and a limited validation of the method are presented in sections 4 and 5 respectively. Once the clear sky longwave flux to the surface is known, the clear sky atmospheric longwave cooling is then determined in the manner described in section 6, where the correlation between the magnitude of this cooling and the column water vapor is also explored.

It remains, however, a considerable challenge to establish meaningful ways of using present-day space measurements to estimate the contributions by clouds to the surface longwave fluxes and therefore to the column heating rates. Despite these unmet challenges, we demonstrate in section 6 of this paper how upper and lower bounds can be placed on these cloud effects and furthermore demonstrate how the longwave effects of clouds in a moist atmosphere, where the column water vapor exceeds approximately 30 kg $m^{-2}$, may be estimated from presently available satellite data with an accuracy of approximately 0.2 K $d^{-1}$. Based on the approach described in section 6, we show how clouds in these relatively moist regions decrease the column cooling by almost 50 % of the clear sky values and we infer the presence of significant gradients of column radiative heating across the equatorial Pacific.

## 2. Data Sources

The main sources of the global data analyzed in this study are those described and used previously in part 3. These data include the ERBE fluxes, the column water vapor retrieved by *Greenwald et al.* [1993] based on passive microwave measurements obtained from the Defense Meteorological Satellite Program's (DMSP) SSM/I instrument [*Hollinger et al.*, 1987], and the sea surface temperature (SST) data of *Reynolds* [1988]. The results from the Colorado State University General Circulation Model (GCM) defined in part 3 are also utilized but more sparingly in this study.

An important new source of data for this study is the simulation of the clear sky longwave radiative fluxes obtained from the system of *Slingo and Webb* [1992] for the simulation and analysis of measurements from satellites using operational analyses (SAMSON). These simulations use initialized analyses from the operational archive at the European Centre for Medium-Range Weather Forecasts (ECMWF) but with the column water vapor constrained to the SSM/I values, as described by *Webb et al.* [1993]. Temperature and specific humidity data on 19 model levels were directly incorporated into the simulations along with analyzed surface pressure.

SAMSON is constructed around a high spectral resolution radiative transfer model [*Shine*, 1991] that incorporates the ECMWF analyses from the operational archive. The accuracy of the radiation model employed

by SAMSON was checked using a single-column version applied to Intercomparison of Radiation Codes for Climate Models (ICRCCM) test profiles [*Ellingson et al.*, 1991]. Calculations of clear sky outgoing longwave radiation (hereafter represented as $F_\infty$) for five standard atmospheres with effects of water vapor, carbon dioxide, and ozone differed from line–by–line calculations of $F_\infty$ by approximately 1 W m$^{-2}$, suggesting excellent agreement with these reference calculations [*Slingo and Webb*, 1992]. Comparison of clear sky values of $F_g$ depends to a small extent on the specific details of how the continuum absorption is dealt with in the model. The treatment of the continuum is described by *Shine* [1991] and is based on the far-wing treatment of *Clough et al.* [1986]. Variations of the treatment of this continuum can introduce uncertainties in calculations of the surface flux up to 10 W m$^{-2}$ [*Ellingson et al.*, 1991]. SAMSON simulations of $F_g$ agreed with reference ICRCCM calculations of this flux within 3 W m$^{-2}$.

For the simulations shown below, the effects of minor trace gases of nitrous oxide, methane, CFC11, and CFC12 were included in addition to water vapor, carbon dioxide and ozone, and the volume mixing ratios of these gases, which are assumed to be uniformly mixed in the atmosphere, are given by *Slingo and Webb* [1992].

The research described in this paper also introduces surface radiation flux data collected during two oceanographic research cruises by the R/V *Alliance* in the Mediterranean Sea off Crete in June 1990 and off Corsica in the fall of 1991 and by the USCGC *Polar Sea* cruise in the Arctic Sea in July and August 1992 [*Minnett*, 1992, 1993; *NEWATER*, 1993]. For the present purposes the relevant data from these cruises consist of measurements of downwelling infrared fluxes at the surface measured by Eppley pyrgeometers mounted on a mast at 16 m above sea level, observed cloud amounts, and concurrent radiosonde data. During the 1990 Mediterranean experiment the ship was overflown on four occasions by the U.K. meteorological research flight C–130 which carried a precision pyrgeometer. The differences between the ship measurements and the aircraft measurements were 7,18,-4, and 4 W m$^{-2}$ which represents 2–5% range of differences from the measured flux.

Surface radiation budget data also collected in support of the Tropical Ocean Global Atmosphere (TOGA) Coupled Ocean Atmosphere Response Experiment (COARE) at four island sites; the atoll of Majuro in the Republic of the Marshall Islands at 7 ° 05' N latitude and 171° 23' E longitude and the islands of Pohnepi and Chuuk in the Federated States of Micronesia at 6° 58' N latitude and 158° 13' E longitude and 7° 27' N latitude and 151° 50' E longitude and the island site of Kavieng 2° 30'S 150° 48'E. In addition to these island sites a site located at Darwin 12° 25'S 130° 51'E, Australia is also used in this study. The details of the TOGA data, its quality control, calibration, and its accessibility will be described in a forthcoming paper by the principal author and is described in the report of *Cornwall et al.* [1993].

## 3. SAMSON Simulations

Simulations of the monthly mean clear sky fluxes over the ice-free oceans were carried out for the period March 1988 to February 1989 which is also a period for which both ERBE and SSM/I observations are available. As in the original study of *Slingo and Webb* [1992], these simulations apply to a horizontal resolution of 5°. The radiation code was applied to each daily analyses (a mean of four 6 hourly analysis for each day) and then averaged to produce the monthly mean flux distributions which are used in the analyses described below. Both *Slingo and Webb* [1992] and *Webb et al.* [1993] discuss the differences between the simulated fluxes from SAMSON and the clear sky values of $F_\infty$ obtained from ERBE. Figure 1 presents examples of scatter diagrams of the SAMSON $F_\infty$ versus the ERBE $F_\infty$ for April, July, and September 1988 and January 1989 to highlight some gross features of these comparisons. For instance, a slight positive bias of 3–5 W m$^{-2}$ exists between the SAMSON and ERBE fluxes, a bias similar in both sign and magnitude to that of the ERBE clear sky flux data [*Harrison et al.*, 1988]. As *Webb et al.* [1993] show, there are regions (not shown) where the differences between the simulated fluxes and the ERBE-derived fluxes exceed this small bias, such as over the areas of marine boundary layer clouds off the west coasts of the major continents where differences may be as large as 10 W m$^{-2}$. These areas can be traced to biases in the ECMWF water vapor data [e.g., *Liu et al.*, 1992; *Stephens et al.*, 1994].

Except for these particular regions the simulations of clear sky $F_\infty$ from SAMSON generally agree with ERBE estimates of this flux to within 5–10 W m$^{-2}$, which is considered to be of the same order of uncertainty of the latter. There are also no a priori reasons to expect the SAMSON simulations of clear sky $F_g$ to be grossly in error although it is noted above how the specific details of how the continuum absorption is modeled may introduce an uncertainty of the order of 10 W m$^{-2}$. Bearing this possibility in mind, simulated distributions of $F_g$ over the ice-free oceans are presented in Plates 1*a* and 1*b* in the form of the surface net flux (i.e., $\sigma T_s^4 - F_g$). The maps of the surface net flux shown in Plates 1*c* and 1*d* are those derived by the approach described below and are presented here for comparison. The smallest net fluxes of around 40–50 W m$^{-2}$ occur in the tropical convergence zones over the Pacific and Indian Oceans and in the Northwest Pacific in July. A significant annual variation close to the northern continents also appears to exist which is associated with changes in the atmospheric circulation associated with the summer and winter monsoons. There is also a close correspondence in the tropics between column-integrated water vapor $w$ (discussed later in relation to Plates 2*c* and 2*d*) and the surface net longwave fluxes shown in Plate 1. This arises because atmospheric temperatures are relatively uniform in the tropics, so the net flux is mainly determined by the lower tropospheric humidities, which also dominate $w$ [e.g., *Stephens*, 1990].

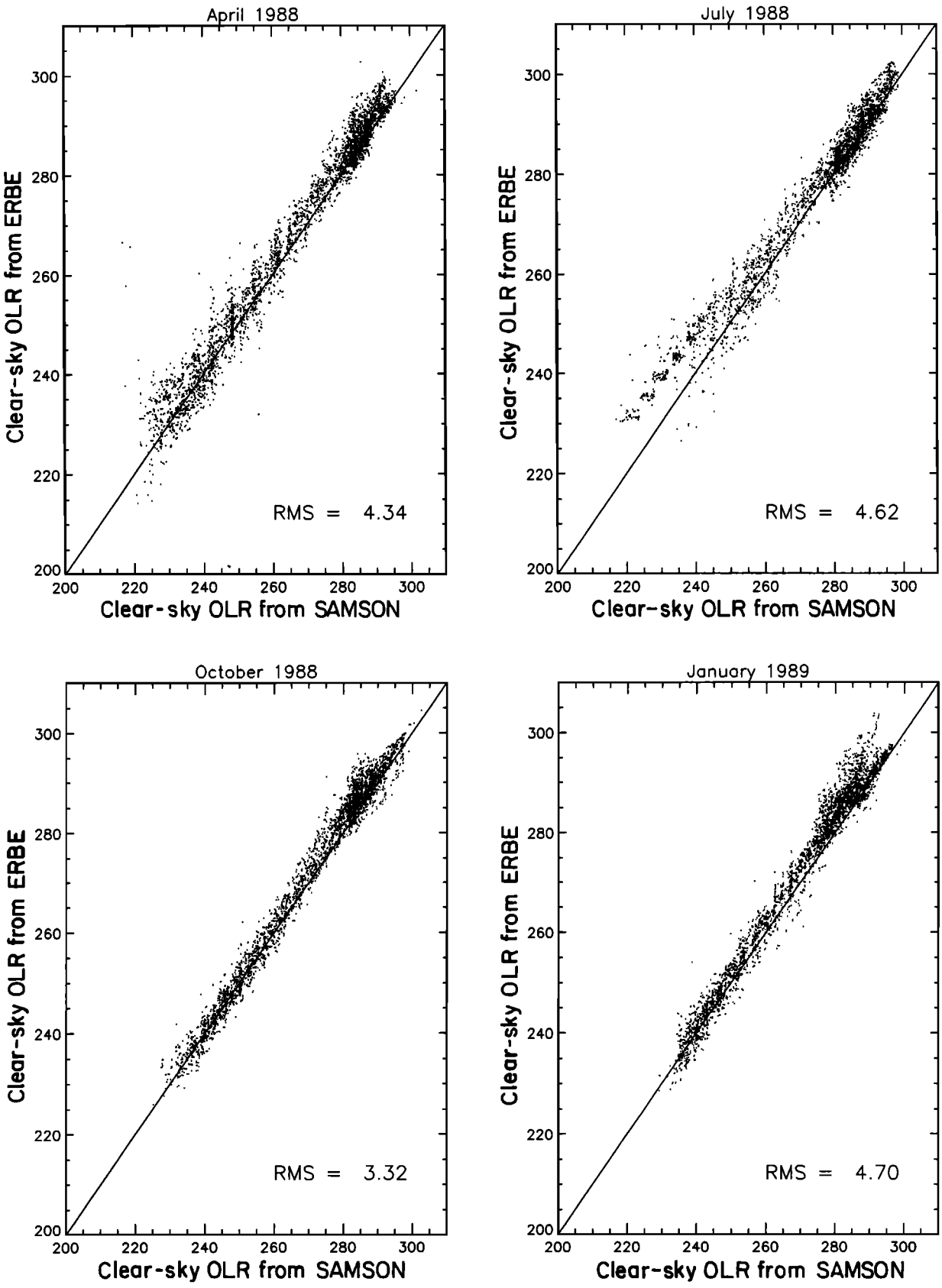


**Figure 1.** Scatter diagrams of (SAMSON) simulated $F_\infty$ versus (ERBE) analyses of clear sky longwave fluxes for April, July, and September 1988 and January 1989.

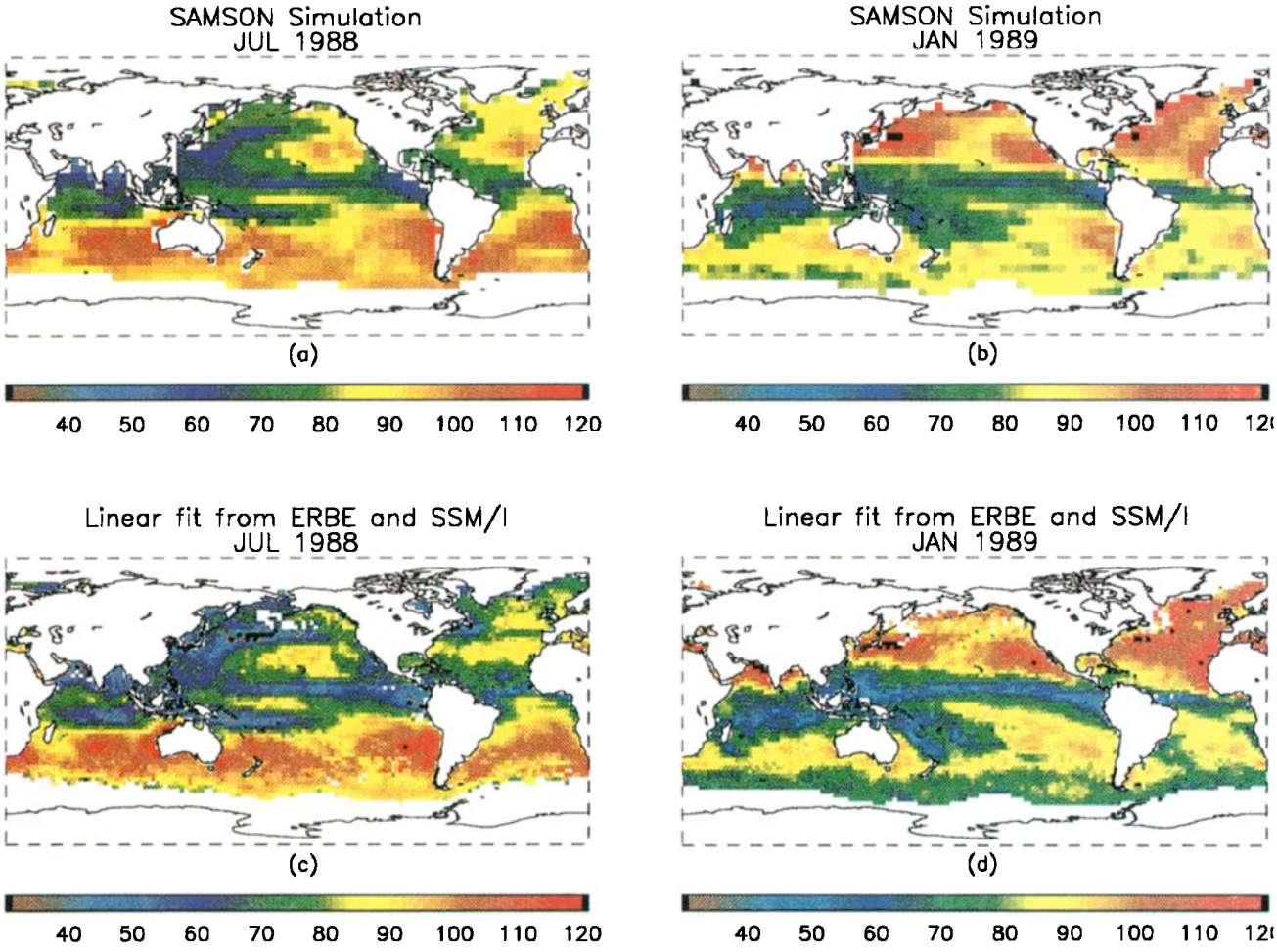


**Plate 1.** (a) and (b) Distributions over the oceans of the July and January SAMSON simulations of surface net longwave flux. (c) and (d) Same as Plates 1a and 1b but the net flux deduced using a linear regression of the flux ratio according to (7b) and ERBE and (SSM/I) precipitable water.

Except at a few isolated locations, there exist very little independent, research-quality data to validate the simulations of $F_g$ shown in Plates 1*a* and 1*b* or the simple retrieval of $F_g$ introduced later and shown in Plates 1*c* and 1*d*. A limited attempt to validate the latter is described below.

## 4. Flux Ratios and a Simple Description of the Planetary Greenhouse Effect

Part 1 introduced a simple model of the clear sky Earth's greenhouse effect. While that model is described briefly in that paper, a more detailed account is given here because a new relationship defined by this model is explored. As in part 1, the model is based on simple considerations of radiative equilibrium and is introduced here merely as a diagnostic guide providing a framework for analyses of the data. Its use should not be misconstrued as an assumption on our part that the Earth's climate exists in such an equilibrium state. The model derives from the radiative transfer equation applicable to a nonscattering atmosphere, namely,

$$\mu \frac{dI(\tau,\mu)}{d\tau} = I(\tau,\mu) - B(T) \tag{1a}$$

$$-\mu \frac{dI(\tau,-\mu)}{d\tau} = I(\tau,-\mu) - B(T), \tag{1b}$$

where $I$ is the intensity, $\mu = \cos\theta$ where $\theta$ is the angle of the beam from the zenith.

The optical depth is defined as

$$\tau = \int_z^\infty k\rho_a dz, \tag{2}$$

where $k$ is the mass absorption coefficient, $\rho_a$ is the density of the absorbing gas and $z$ is the lowest end point of the path. Casting (1a) and (1b) into equations for upward ($F^\uparrow$) and downward ($F^\downarrow$) hemispheric fluxes leads to

$$\frac{dF^\uparrow}{d\tilde{\tau}} = F^\uparrow - \pi B, \tag{3a}$$

$$-\frac{dF^\downarrow}{d\tilde{\tau}} = F^\downarrow - \pi B, \tag{3b}$$

where

$$\tilde{\tau} = \frac{3}{2}\tau. \tag{4}$$

If we apply these equations to the broad band, then $\sigma T^4$ replaces $\pi B$ and $\tilde{\tau}$ is taken to be a gray body optical depth. Radiative equilibrium then implies that

$$F^{\uparrow}(\tilde{\tau} = 0) = Q_o(1 - \alpha) = F_{\infty},$$

where $Q_o$ is the global annual–mean incoming solar radiation at the top of the atmosphere and $\alpha$ is the planetary albedo. It also follows that

$$F_{net} = F^{\uparrow}(\tilde{\tau}) - F^{\downarrow}(\tilde{\tau}) = \text{constant}$$

which leads to the solution of (3a) and (3b) as

$$\sigma T_s^4 = \frac{F_{\infty}}{2}[2 + \tilde{\tau}_s] \tag{5a}$$

$$F_g = F^{\downarrow}(\tilde{\tau}_s) = \frac{F_{\infty}}{2}\tilde{\tau}_s \tag{5b}$$

where $\tau = \tau_s$ and $\tilde{\tau} = \tilde{\tau}_s$.

Part 1 uses (5a) to introduce a parameter $\mathcal{G}$ in the form

$$\mathcal{G} = \frac{\sigma T_s^4}{F_{\infty}} = a + b\tau_s, \tag{6a}$$

which is taken to be a measure of the strength of the planetary greenhouse effect where from (5a) and (4), $a$=1 and $b$=3/4. In a similar way the relationship (5b) provides a second flux relationship

$$\mathcal{F} = \frac{F_g}{F_{\infty}} = b\tau_s \tag{6b}$$

which we explore in further detail in the next section.

The flux ratio quantity given in (6a) is not only a convenient measure of the planetary greenhouse effect but it also identifies the gray body optical depth as a crucial parameter is defining the magnitude of this effect. It was also shown in part 1 that under clear sky conditions, a proportional relation between $\mathcal{G}$ and the column-integrated water vapor exists and has the form

$$\mathcal{G} = a_1 + c_1 w. \tag{7a}$$

The advantage of (7a) over other definitions is that all factors in (7a) may be independently observed over the global oceans using current satellite observations and so its viability can be tested. For example, $\mathcal{G}$ is calculated from the SST which is available from blended analyses of ship, buoy, and satellite data [e.g., *Reynolds*, 1988] and from the clear sky $F_{\infty}$ which is available from ERBE data prior to 1991. The column water vapor amount $w$ is also available over the oceans from microwave measurements obtained from the SSM/I, which have flown on the DMSP satellites since 1987. Using these data, we determine the coefficients in (7a) are $a_1 = 1.39$ and $c_1 = 0.005$ kg$^{-1}$ m$^2$.

Similarly, (6b) leads us to suppose that a simple relation exists between $\mathcal{F}$ and precipitable water $w$ of the form

$$\mathcal{F} = a_2 + c_2 w \tag{7b}$$

in an entirely analogous way to (7a) where $a_2 = 0.937$ and $c_2 = 0.0102$ kg$^{-1}$m$^2$. Unfortunately, we do not have global observations of $F_g$ and thus we cannot derive $\mathcal{F}$ solely from independent observations to test this relationship. We propose to use the flux simulations of SAMSON in lieu of these much needed observations.

### 4.1. Results

Scatter plots of $\mathcal{G}$ derived from ERBE clear sky $F_{\infty}$ satellite data and from SAMSON simulations of the clear sky $F_{\infty}$ are compared in Figures 2a and 2b for July and Figures 2c and 2d for January 1989. In this diagram, $\mathcal{G}$ is plotted as a function of SST rather than of $w$, as described previously in part 1 and *Webb et al.* [1993] and *Stephens et al.* [1993]. When plotted in this way, a dramatic branching of the relation between $\mathcal{G}$ and SST appears which *Webb et al.* [1993] identify as largely due to a seasonal effect associated with changes in the vertical profile of atmospheric temperature in the middle latitudes.

The flux ratio quantity $\mathcal{F}$ derived from the same SAMSON simulations presented in Figure 2b are also given in Figure 3a. Similar flux ratios derived from monthly mean clear sky flux data obtained from simulations of the UKMO climate model are also shown in Figure 3b. The results from both sets of data show a well-defined relationship between the flux ratio and $w$ and how this relationship is approximately linear, as predicted by (7b) for $w > 20$ kg m$^{-2}$. The model results exhibit a similar relationship between $\mathcal{F}$ and $w$ and more clearly show its nonlinear but well–behaved character when $w < 20$ kg m$^{-2}$ which resembles the well–known characteristics of the curve of growth of emission as $w$ increases.

A simple linear fit applied over the range $w > 20$ kg m$^{-2}$ was carried out to determine the coefficients $a_2$ and $c_2$ of (7b). The values of these coefficients are given in Figure 3a and together with SSM/I observations of $w$ and ERBE observations of the clear sky $F_{\infty}$ are then used to obtain monthly mean values of $F_g$ over the oceans. Examples of the results of this simple retrieval are presented in Plates 1*c* and 1*d* in the form of the net longwave flux at the ocean surface. These distributions are directly comparable with the SAMSON simulations of net flux shown in Plates 1*a* and 1*b* although the higher spatial resolution of both the ERBE data and the SSM/I precipitable water data allows us to produce results in Plates 1*c* and 1*d* at a resolution of 2.5° × 2.5° compared to the 5° × 5° resolution of the SAMSON data. Despite this difference the retrieved distributions are both qualitatively and quantitatively very similar to those of SAMSON. The rms difference between the retrieved and the simulated fluxes is ±6 W m$^{-2}$, which is considerably smaller than the uncertainty presently expected from the direct radiometric measurements of this flux [*Dutton*, 1993]. We interpret this rms difference as a confirmation the viability of the method.

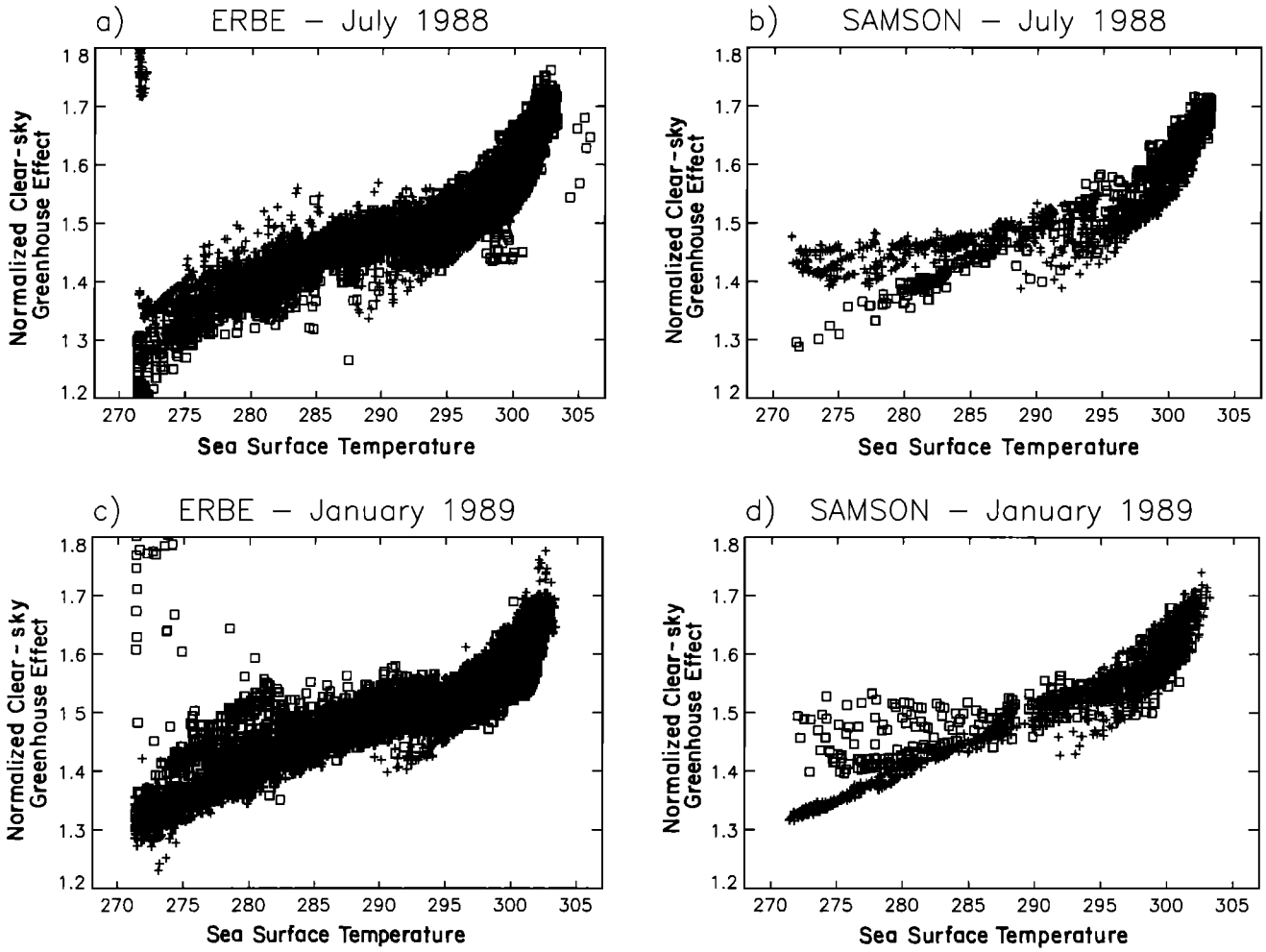


**Figure 2.** (a) The derived $\mathcal{G}$ from ERBE data and the Reynolds (SST) data as a function of SST for July 1988.(b) The corresponding relation using SAMSON values of $F_\infty$. (c) and (d) Same as Figures 2a and 2b but for January 1989 defined using SAMSON simulations of $F_\infty$.

### 4.2. Simple Interpretation of Flux Ratios

*Webb et al.* [1993] provide a simple analysis of the influences of the bulk effects of lapse rate on $\mathcal{G}$. Here we extend this analyses to $\mathcal{F}$ and consider how other factors can also potentially influence $F_\infty$ independent of any significant change in $w$. In this way we offer a relatively simple framework for understanding some factors that produce the scatter in the relationships depicted in Figures 2a and 2b and Figures 3a and 3b. For example, increasing water vapor in the middle and upper troposphere only marginally affects $w$ but may significantly alter $F_\infty$. With all other factors fixed, increasing (decreasing) upper tropospheric moisture leads to respective decreases (increases) in $F_\infty$ and thus to an increase (decrease) in $\mathcal{G}$. Similarly, variations in the vertical profile of temperature also alter $F_\infty$ and thus $\mathcal{G}$. For example, a warmer (colder) atmospheric column (assuming water vapor as fixed) leads to an increase (decrease) in $F_\infty$ and thus to a decrease (increase) in $\mathcal{G}$. These two factors, we argue, are principally responsible for producing the observed scatter.

Here we adapt and extend the simple model introduced by *Webb et al.* [1993] to explore the sensitivities of both $\mathcal{G}$ and $\mathcal{F}$ to variations in the vertical profiles of both temperature and moisture. Consider a single-layer atmosphere, as shown in the left portion of Figure 4. The upwelling radiation from the top of this atmosphere is $F_\infty$ and the downwelling radiation at the base is $F_g$. These fluxes may be simply related to the radiating temperature of the atmosphere $T_a$ (roughly the 800-mbar temperature), the emissivity of the layer $\varepsilon_a$, and the SST $T_s$ via the approximate transfer equations

$$F_\infty = (1-\varepsilon_a)\sigma T_s^4 + \varepsilon_a \sigma T_a^4$$

$$F_g = \varepsilon_a \sigma T_a^4$$

which on substitution into (6a) and (6b) and with some rearrangement give

$$\mathcal{G} = \frac{1}{1-\varepsilon_a[1-(T_a/T_s)^4]} \tag{8a}$$

$$\mathcal{F} = \frac{\varepsilon_a (T_a/T_s)^4}{1-\varepsilon_a[1-(T_a/T_s)^4]}. \tag{8b}$$

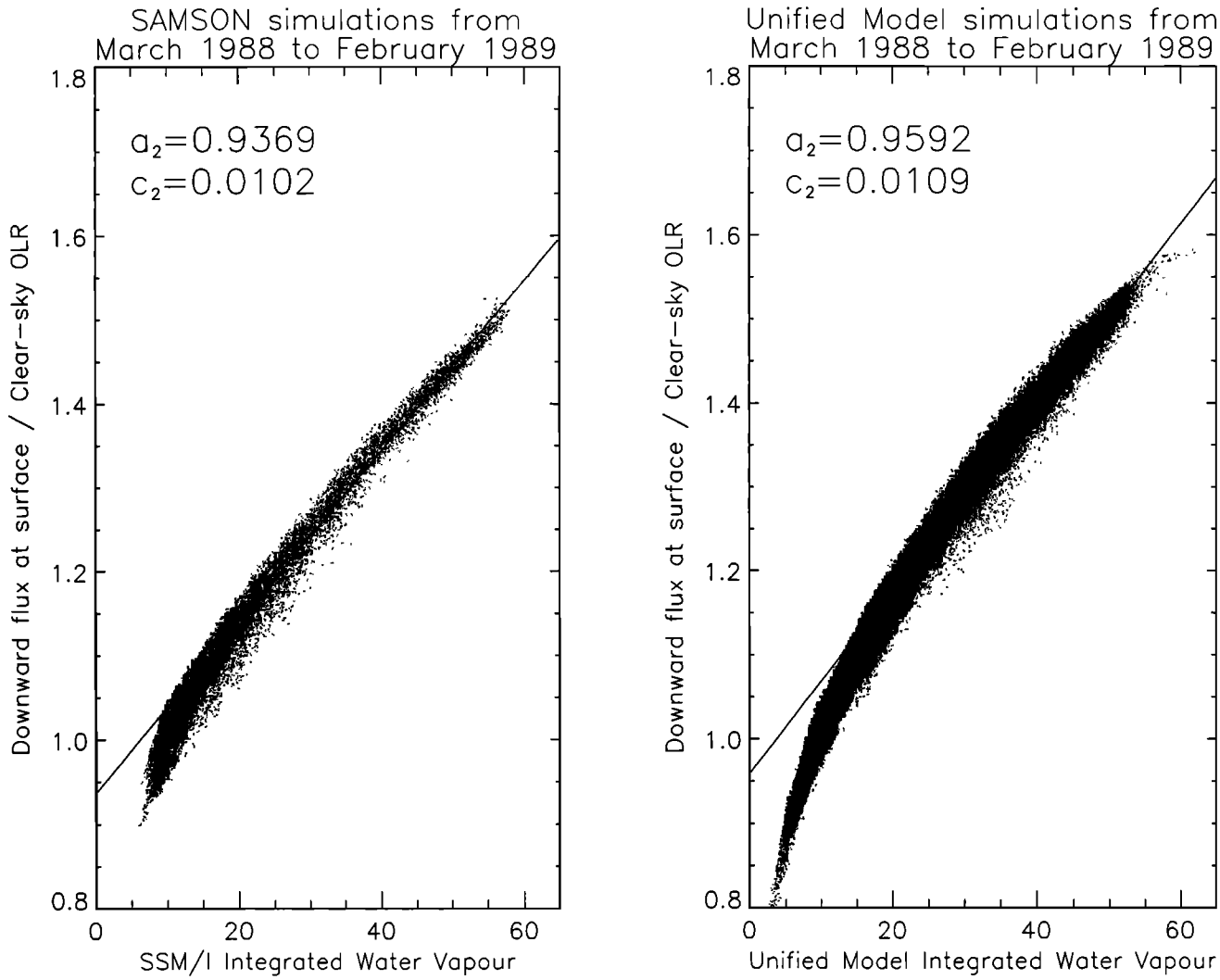


**Figure 3.** The flux ratio $\mathcal{F}$ derived from combined SAMSON simulations of January and July fluxes as a function of $w$. (b) As in Figure 3a but for the flux ratio derived using monthly mean clear sky fluxes from (CSU GCM) simulations.

Two important factors govern the behavior of both ratio quantities in these expressions, namely, the temperature profile which we associate with the temperature ratio $T_a/T_s$ and the total column water vapor which is implied in $\varepsilon_a$. *Webb et al.* [1993] using (8a) demonstrated that the branching of the relationship between $\mathcal{G}$ and SST when $T_s$ <285 K occurs through changes in $T_a/T_s$ from summer to winter. During winter the lapse rate in these regions is increased (we think of this as a reduction in $T_a/T_s$ relative to summertime conditions) and this increase in turn produces smaller values of the denominator and hence larger values of $\mathcal{G}$ relative to summertime conditions. Conversely, larger values of $w$ lead to larger values of $\varepsilon_a$, a smaller denominator and thus a larger $\mathcal{G}$ which is consistent with (7a).

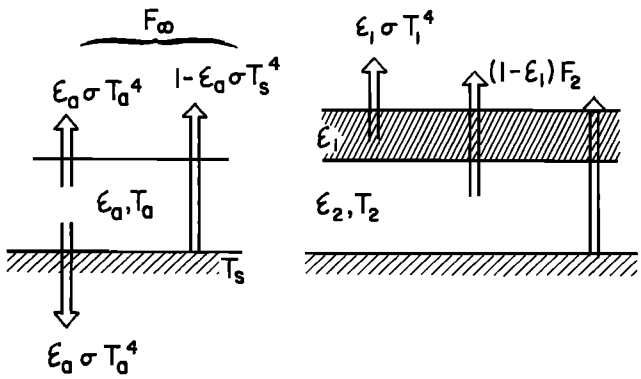


**Figure 4.** (left) A simple-single layer atmosphere used to highlight sensitivities in flux ratio quantities (right) and a two-layer atmosphere used to identify effects of upper tropospheric moisture.

The effect of temperature on $\mathcal{F}$ is not so simple to diagnose as are the effects of temperature on $\mathcal{G}$ since the $T_a/T_s$ factor appears in both the denominator and the numerator of (8b). We infer from this simple expression that the effects of changing $T_a/T_s$ are largely canceled in this ratio.

To illustrate possible effects of the vertical structure of moisture on these ratios in a simple way, consider a two-layer atmosphere, as shown to the right of Figure 4. The properties of each layer are labeled as shown on this diagram. The fluxes to space and to the surface

simply follow as

$$F_\infty = (1-\varepsilon_1)F_2 + \varepsilon_1\sigma T_1^4$$

$$F_g = (1-\varepsilon_2)\varepsilon_1\sigma T_1^4 + \varepsilon_2\sigma T_2^4$$

where

$$F_2 = (1-\varepsilon_2)\sigma T_s^4 + \varepsilon_2\sigma T_2^4.$$

A change in these fluxes due to a change in the water vapor path will be denoted as $\Delta F^{(1),(2)}$ depending on whether this change occurs either in the top layer 1 or the bottom layer 2, respectively. It is trivial to show that these flux changes are

$$\Delta F_\infty^{(1)} = \Delta\varepsilon_1[\sigma T_1^4 - F_2]$$

$$\Delta F_\infty^{(2)} = \Delta\varepsilon_2(1-\varepsilon_1)[\sigma T_2^4 - \sigma T_s^4]$$

and that

$$\Delta F_g^{(1)} = \Delta\varepsilon_1(1-\varepsilon_2)\sigma T_1^4$$

$$\Delta F_g^{(2)} = \Delta\varepsilon_2[\sigma T_2^4 - \varepsilon_1\sigma T_1^4]$$

for a given change in layer emissivity that occurs as a result of respective changes in water vapor path. The change in flux ratios due to these path changes is then

$$\frac{\Delta\mathcal{F}}{\mathcal{F}} = \frac{\Delta F_g}{F_g} - \frac{\Delta F_\infty}{F_\infty}$$

$$\frac{\Delta\mathcal{G}}{\mathcal{G}} = -\frac{\Delta F_\infty}{F_\infty}.$$

Estimates of the flux changes $\Delta F_\infty^{(1),(2)}$ and $\Delta F_g^{(1),(2)}$ together with the changes in the ratios $\Delta\mathcal{F}^{(1),(2)}/\mathcal{F}$ and $\Delta\mathcal{G}^{(1),(2)}/\mathcal{G}$ are given in Table 1 based on radiative transfer calculations using the two-stream model of *Stackhouse and Stephens* [1991] applied to the *McClatchey et al.* [1972] midlatitude summer atmosphere. In these calculations we have taken layer 2 to represent the layer from the surface to approximately 500 mbar with a path $u_1 = 28.2$ mm and layer 1 to represent the layer above 500 mbar with $u_2 = 1.8$ mm. The quantities given in the table are derived for a specified change in layer emissivities and the parameter values given. The emissivity values given were derived from the formulae of *Rodgers* [1967] and the quoted changes in emissivity are a result of 10% changes in $u_1$ and $u_2$, respectively. According to these results a 10% change in upper tropospheric moisture (i.e., an increase in $u_1$ of 0.2 mm) has a threefold larger effect on $F_\infty$ than does an equivalent percentage change (but significantly larger absolute change of 2.8 mm) in lower tropospheric water vapor. This is due to a combination of the nonlinear curve of growth of emissivity as a function of $u$ where small changes in path in an existing dry layer leads to a larger change in emissivity than occurs when the path of moist layer is increased by the same amount. This feature is indicated by the a factor of 2 difference in $\Delta\varepsilon$ listed in the table. This disproportionate influence of upper tropospheric moisture on $F_\infty$ and, subsequently, on $\mathcal{G}$ has also been noted by others in a slightly different context [e.g., *Shine and Sinha,* 1991]. According to the results listed in Table 1, changes in upper tropospheric moisture, which go undetected by sensors such as the SSM/I, can also affect $\mathcal{F}$ and it is reasonable to expect that the scatter in the relationship shown in Figure 3 is due to variations in the moisture profile, including changes in the upper tropospheric moisture that are not necessarily reflected in variations in $w$.

**Table 1.** Changes in Fluxes and Flux Ratios

| $\Delta\varepsilon_1$ | $\Delta\varepsilon_2$ | $\Delta F_\infty$ | $\Delta F_g$ | $\Delta\mathcal{G}/\mathcal{G}$ | $\Delta\mathcal{F}/\mathcal{F}$ |
|---|---|---|---|---|---|
| 0.02 | ··· | -1.4 | 0.8 | 0.005 | 0.007 |
| ··· | 0.01 | -0.48 | 1.8 | 0.0017 | 0.0066 |

The values in this table were derived for the following: $\sigma T_s^4 = 423$, $F_\infty = 289$, $F_g = 338$, $F_2^\uparrow(\approx F_{500mb}^\uparrow) = 338$, $F_2^\downarrow(\approx F_{500mb}^\downarrow) = 139$, $u_2 = 28.2$, $u_1 = 1.8$, $\varepsilon_1 = 0.85$, $\varepsilon_2 = 0.52$ where the fluxes are in W m$^{-2}$ and the path quantities are in mm.

## 5. Validation of the $\mathcal{F}$ Ratio

The $\mathcal{F}$–$w$ relationship shown above is now checked using both independent surface longwave flux measurements and concurrent radiosonde data. These observational data were obtained from both ship-borne and island-based measurements, but unfortunately they were available only after the failure of the ERBE scanning radiometers. Thus the clear sky values of $F_\infty$ used to derive the ratio $\mathcal{F}$ were obtained from radiative transfer calculations using the column version of the SAMSON and profile information prescribed by the radiosonde data collected at the measurement site as input.

The surface flux data were first analyzed to identify clear sky periods and the fluxes at these times were then averaged to produce 30-min averaged fluxes. Coincident ship-borne observer reports of cloudiness were used to determine these clear sky conditions which were

**Table 2a.** Monthly Mean Infrared Fluxes

| Cruise | $F_g$ | $F_\infty$ | $w$ | $\mathcal{F}$ |
|---|---|---|---|---|
| Mediterranean | 315 | 293 | 19 | 1.074 |
| | 355 | 313 | 18 | 1.133 |
| | 340 | 321 | 20 | 1.060 |
| | 360 | 324 | 21 | 1.112 |
| | 350 | 317 | 21 | 1.104 |
| | 360 | 320 | 23 | 1.125 |
| | 345 | 319 | 19 | 1.081 |
| | 350 | 323 | 17 | 1.083 |
| | 335 | 316 | 20 | 1.060 |
| | 355 | 319 | 20 | 1.112 |
| | 335 | 305 | 21 | 1.096 |
| | 375 | 302 | 26 | 1.241 |
| Arctic | 250 | 260 | 13 | 0.961 |
| | 235 | 259 | 11 | 0.906 |
| | 225 | 249 | 7 | 0.904 |
| | 220 | 248 | 7 | 0.887 |
| | 210 | 250 | 6 | 0.840 |
| | 225 | 247 | 7 | 0.904 |

Monthly mean (mm) infrared fluxes (in W m$^{-2}$) and colocated sonde precipitable water content (in mm) measured during two cruises. Calculated values of $F_\infty$ are also presented.

**Table 2b. Monthly Mean and Standard Deviation of the Infrared Fluxes**

| | | All Sky | | | | | Clear Sky | | | | | |
|---|---|---|---|---|---|---|---|---|---|---|---|---|
| Site | Month | $F_g$ | $\sigma_F$ | w | $\sigma_w$ | N | $F_g$ | $\sigma_F$ | w | $\sigma_w$ | N | $F_\infty$ |
| Chuuk | 12/92 | 405.0 | 11.7 | 40.7 | 7.1 | 8 | 399.4 | 2.0 | 41.4 | 10.4 | 3 | 298.7 |
| | 1/93 | 417.4 | 15.2 | 48.2 | 11.0 | 29 | 407.0 | 9.5 | 44.5 | 9.5 | 9 | 300.9 |
| | 2/93 | 414.0 | 11.4 | 45.8 | 10.2 | 25 | 411.0 | 8.7 | 43.7 | 7.0 | 12 | 295.6 |
| Majuro | 12/92 | 423.0 | 11.7 | 46.0 | 9.6 | 22 | 411.6 | 9.7 | 40.4 | 7.1 | 6 | 309.4 |
| | 1/93 | 427.4 | 12.8 | 51.6 | 10.7 | 27 | 419.5 | 12.3 | 45.4 | 9.9 | 8 | 300.1 |
| | 2/93 | 422.8 | 15.1 | 47.5 | 11.2 | 24 | 408.7 | 9.7 | 38.7 | 8.0 | 10 | 299.5 |
| Kavieng | 1/93 | 443.9 | 6.0 | 52.6 | 3.4 | 6 | 441.4 | 0.5 | 54.0 | 0.2 | 2 | 284.2 |
| | 2/93 | 435.6 | 4.6 | 53.3 | 4.9 | 25 | 433.9 | 2.8 | 51.6 | 3.8 | 11 | 288.1 |
| Darwin | 12/92 | 446.7 | 9.7 | 46.4 | 6.3 | 20 | 451.1 | 4.7 | 42.1 | 6.2 | 6 | 302.6 |
| | 1/93 | 447.6 | 9.9 | 52.9 | 8.4 | 29 | 449.0 | 10.0 | 47.7 | 6.6 | 11 | 296.0 |
| | 2/93 | 441.6 | 7.3 | 50.5 | 5.4 | 24 | 441.5 | 9.6 | 48.9 | 4.7 | 7 | 286.6 |

Monthly mean and standard deviation of the infrared fluxes (in W $m^{-2}$) and co-located sonde precipitable water content and standard deviation (in mm) during TOGA/COARE. The fluxes indicated by the superscript 's' are those derived from SAMSON.

defined when cloud amounts of 3/10 cloudiness or less prevailed during the time of measurement. The flux measurements, simulated values of $F_\infty$, the values of $w$ derived from the radiosondes as well as values of the flux ratio are given in Table 2a. Simulated values of $F_g$ are not given but the rms differences between these simulated fluxes and measured fluxes is 12.7 and 9.4 W $m^{-2}$ for the Mediterranean and Arctic measurements, respectively.

Surface observations of cloudiness over the island sites were not available at the time of the analyses reported here, so a method was established for identifying clear skies based on the measurements of the accompanying solar flux data. The effects of possible cloud contamination in the day time TOGA data are not considered to be a significant problem since most cloudiness conditions could be readily identified in the solar flux time series and even deep clouds produce only a relatively small change in the longwave flux in the moist conditions that prevail at the TOGA island sites. The more subtle effects of broken clouds or thin clouds that are more difficult to detect in the surface solar flux measurements also have little effect on the measurements of $F_g$. Table 2b presents the longwave fluxes measured at the TOGA sites separated into all-sky and clear sky conditions and provides the SAMSON simulation of $F_\infty$ and the derived flux ratio for clear sky conditions. The simulated fluxes of $F_g$ are also not presented in this table and the rms differences between the measured and the simulated values of $F_g$ fluxes are within 10 W $m^{-2}$ for these TOGA stations. The data in Table 2b support the assertion that the higher-moisture content of the tropical atmosphere masks the effects of emission from clouds measured at the surface. This may be seen from the difference between cloudy and clear sky fluxes obtained from the subtraction of all-sky fluxes $F_g$ and $F_g$ obtained under clear sky conditions as well as the standard deviations of each of these fluxes. The smallness of both the flux differences and their variability is consistent with the notion that the effects of partially cloudy skies which may be incorrectly diagnosed as clear skies are not likely to be significantly larger than 10 W $m^{-2}$.

Values of the flux ratio $\mathcal{F}$ obtained from the measurements of $F_g$ and the simulations of $F_\infty$ are presented in both Figure 5 as well as in Tables 2a and 2b as a function of the radiosonde derived precipitable water $w$. Ratio values for the Arctic, Mediterranean and tropical Pacific are identified in Figure 5 by different symbols. The linear regression of the SAMSON simulations taken from Figure 3a is also shown in the diagram (dashed line) for reference as well as simulated ratios obtained with the SAMSON radiative transfer model and five *McClatchey et al.* [1972] model atmospheres. The latter calculations, indicated by pluses connected by lines, are the results of a series of three calculations carried out for each of the five model atmospheres. The water vapor profiles of these atmospheres was multiplied at each level by one of three constant factors (0.75, 1.0, and 1.25, respectively). These calculations provide a reference for comparison with the measurements, espe-

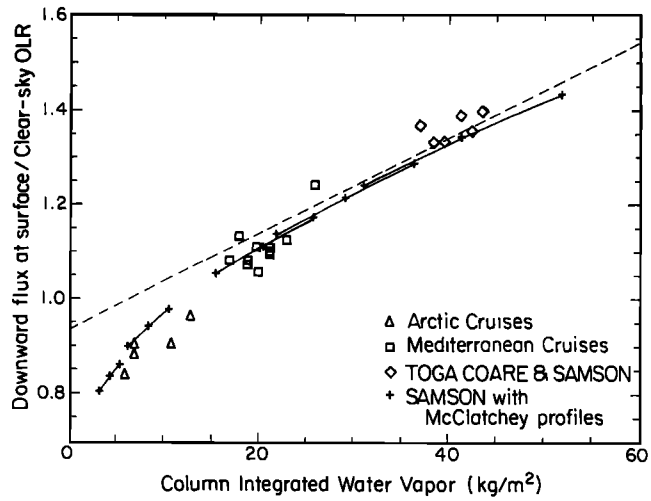


**Figure 5.** The flux ratio $\mathcal{F}$ as a function of $w$ for model-derived relationships (points connected by lines), the regression line derived from the results of Figure 3a and from the measurements indicated.

cially those over the Arctic where the values of $w$ are smallest and the relationship between $\mathcal{F}$ and $w$ is most nonlinear. The calculations using these model atmospheres produce a relationship that also closely fits both the SAMSON regression relation and the flux ratio data measurements. The agreement between the two modeled relationships and the data is offered as a form of validation of the $\mathcal{F}$–$w$ relationship.

## 6. Column Infrared Cooling Rates

The loss of longwave radiative energy by the atmosphere is governed by the emissions of infrared radiation from the atmosphere to space and toward the surface. We can define this loss in terms of the following infrared budget:

$$\Delta F = (\sigma T_s^4 - F_\infty - F_g), \tag{9}$$

where the first term of the right hand side is given by the SST data,

the second term is derived from ERBE measurements and the third term in the balance follows from (7b) using values of the parameters $a_2$ and $c_2$ derived from SAMSON together with satellite observations of $w$ and $F_\infty$ for clear sky conditions.

### 6.1. Clear Sky Cooling Rates

It is common to express the loss of radiant energy by the atmosphere as the rate of cooling of the atmospheric column which follows from (9) as

$$\frac{dT}{dt} = \frac{g}{c_p p_s}\Delta F \tag{10}$$

where $g$ is the acceleration due to gravity, $c_p$ is the specific heat of air at constant pressure and $p_s$ is the surface pressure. After rearrangement the column heating becomes

$$\frac{dT}{dt} = \frac{gF_\infty}{c_p p_s}[\mathcal{G} - \mathcal{F} - 1], \tag{11}$$

where according to (7a) and (7b) the two terms in brackets vary in a systematic way with $w$. Furthermore for a given $w$ the heating of the column varies proportionally with the clear sky outgoing longwave radiation $F_\infty$ which is a result consistent with the empirical findings obtained from balloon measurements of radiative fluxes by *Sabatini and Suomi* [1962].

We use our retrieval strategy to estimate clear sky values of $F_g$ from satellite measurements of $F_\infty$ and $w$ as described above and substitute a value of 1013 mbar for $p_s$ and use the monthly mean SST of Reynolds for $T_s$ in (10) and (11) to arrive at monthly mean distributions of the column-averaged clear sky heating rates shown in Plates 2*a* and 2*b* (negative values represent cooling) for July 1988 and January 1989, respectively. A reasonable estimate of the uncertainty of the monthly averaged values of $F_\infty$ and $F_g$ is $\pm 10$ W m$^{-2}$ based on published estimates in ERBE clear sky flux uncertainties and in the uncertainties in $F_g$ expressed by the rms differences discussed in relation to the comparisons shown in Plate 1. These flux uncertainties in turn imply an uncertainty of approximately $\pm 0.2$ K d$^{-1}$ in the column cooling rate. The SSM/I fields of $w$ for July 1988 and January 1989 which are used to produce these heating rate distributions are also shown in Plates 2*c* and *d* for comparison. It is evident that the clear sky column heating rate distributions resemble the distributions of $w$ which is consistent with (11) and the relationship among $\mathcal{G}$, $\mathcal{F}$, and $w$. The largest coolings occur in the moist equatorial regions and in the areas of moisture convergence over the northwest Pacific and Atlantic Oceans during July as well as in the South Pacific convergence zone.

The association between the column-averaged heating rate and $w$ is explored further in Figures 6a and b, where the data displayed in Plates 2*a* and *c* and 2*b* and *d* respectively, are plotted against each other. Based on (11) and the relationships assumed in (7a) and (7b), we expect the cooling rate to increase in an approximate linear way with increasing $w$, as shown in Figures 6*a* and 6*b*. Linear fits of both $\mathcal{F}$ and $\mathcal{G}$ as a function of $w$ yield the following slope coefficients: $c_2 = 0.01015$ (kg m$^{-2}$)$^{-1}$ and $c_1 = 0.00524$ (kg m$^{-2}$)$^{-1}$, respectively, which according to (11) implies a slope of -0.005 (kg m$^{-2}$)$^{-1}$. An example of a relationship with this slope, defined using the global-mean value $F_\infty = 266$ W m$^{-2}$ is also given on each diagram for reference. The column cooling rate deviates from this simple linear dependence on $w$ in such a way that the rate of increase of column cooling with increasing $w$ above about 40 kg m$^{-2}$ decreases.

When the column cooling rate is expressed as a function of SST rather than as a function of $w$, as it is shown in Figures 6*c* and 6*d*, a number of features emerge. The first is the general change in the cooling SST slope for SST exceeding approximately 295 K due to the rapid increase in $w$ as the SST increases beyond this value. The second feature that emerges from Figures 6*c* and 6*d* are the winter–summer hemispheric branches in the column cooling similar to those noted in the $\mathcal{G}$–SST relationship. The characteristics of the relation between the column cooling rate and the SST, especially the increased rate of cooling with increasing SST, may be better understood by reference to Figure 7. This diagram presents scatter diagrams of fluxes as a function of SST. The left panels are $F_\infty$ and $F_g$ derived from satellite data for July 1988 (left panels) as a function of SST and the matching fluxes derived from SAMSON are shown to the right. We can deduce that the enhanced rate of change of cooling for SSTs greater than about 295 K is a result of the enhanced emission from the atmosphere to the surface associated with the increasing water vapor with SST at these temperatures. The rate of increase of emission from the atmosphere as the SST increases exceeds the rate of change of the emission from the surface (i.e., $\sigma T_s^4$). The latter is represented by the solid line in the bottom two panels of Figure 7. For the SST$>$ 290 K, we deduce that $\Delta F_g/\Delta\text{SST} \approx 15$ W m$^{-2}$ K$^{-1}$ and that $\Delta\sigma T_s^4/\Delta\text{SST} \approx 6$ W m$^{-2}$ K$^{-1}$.

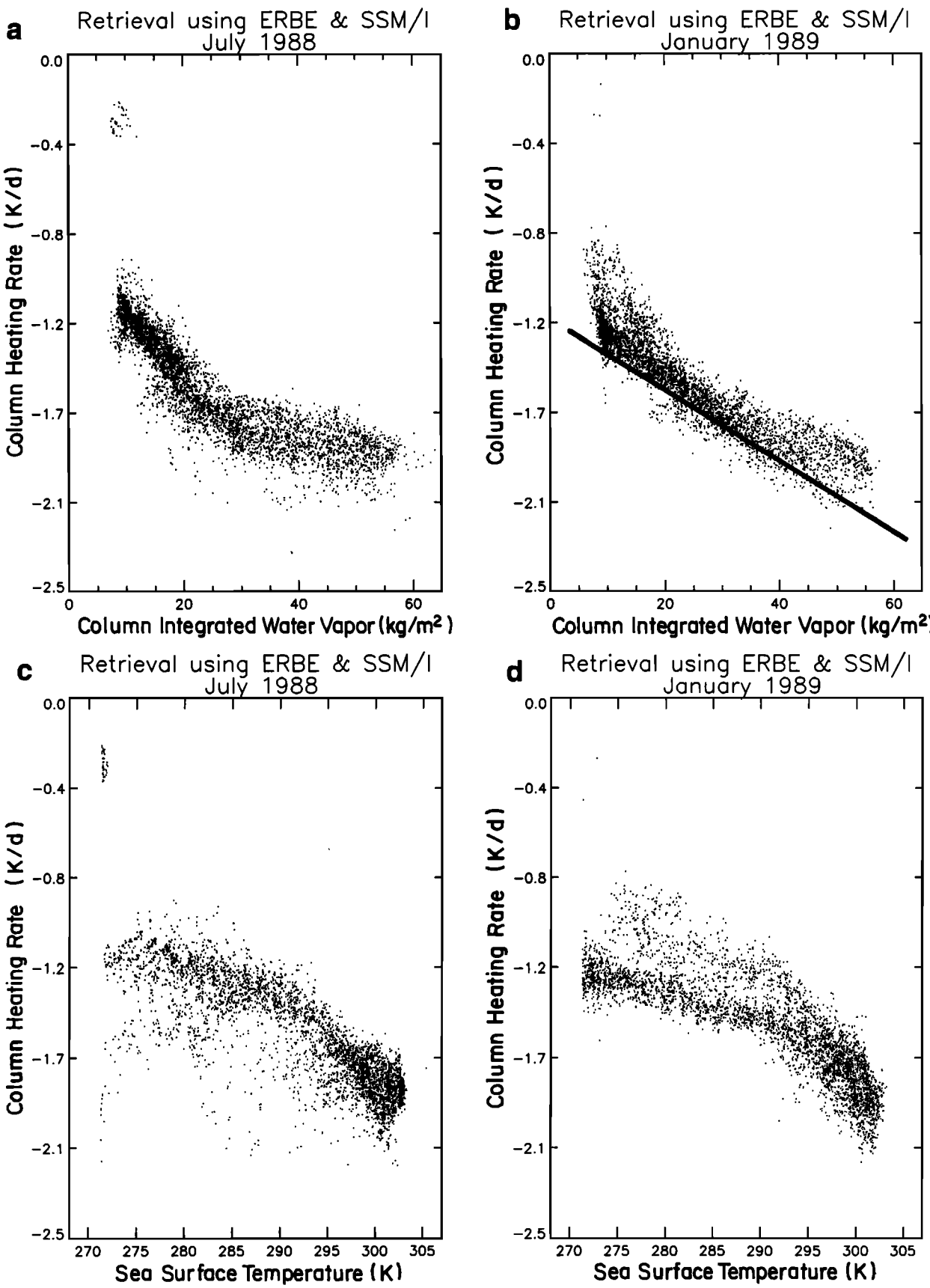


**Figure 6.** The clear sky column cooling rate correlated with the SSM/I-derived column water vapor obtained from the data of (a) July 1988 and (b) January 1989. The solid line are simple linear relationships implied by equations (11), (7a), and (7b) and $F_\infty = 266$ W m$^{-2}$. The clear sky column cooling rate correlated with SST for (c) July 1988 and (d) January 1989.

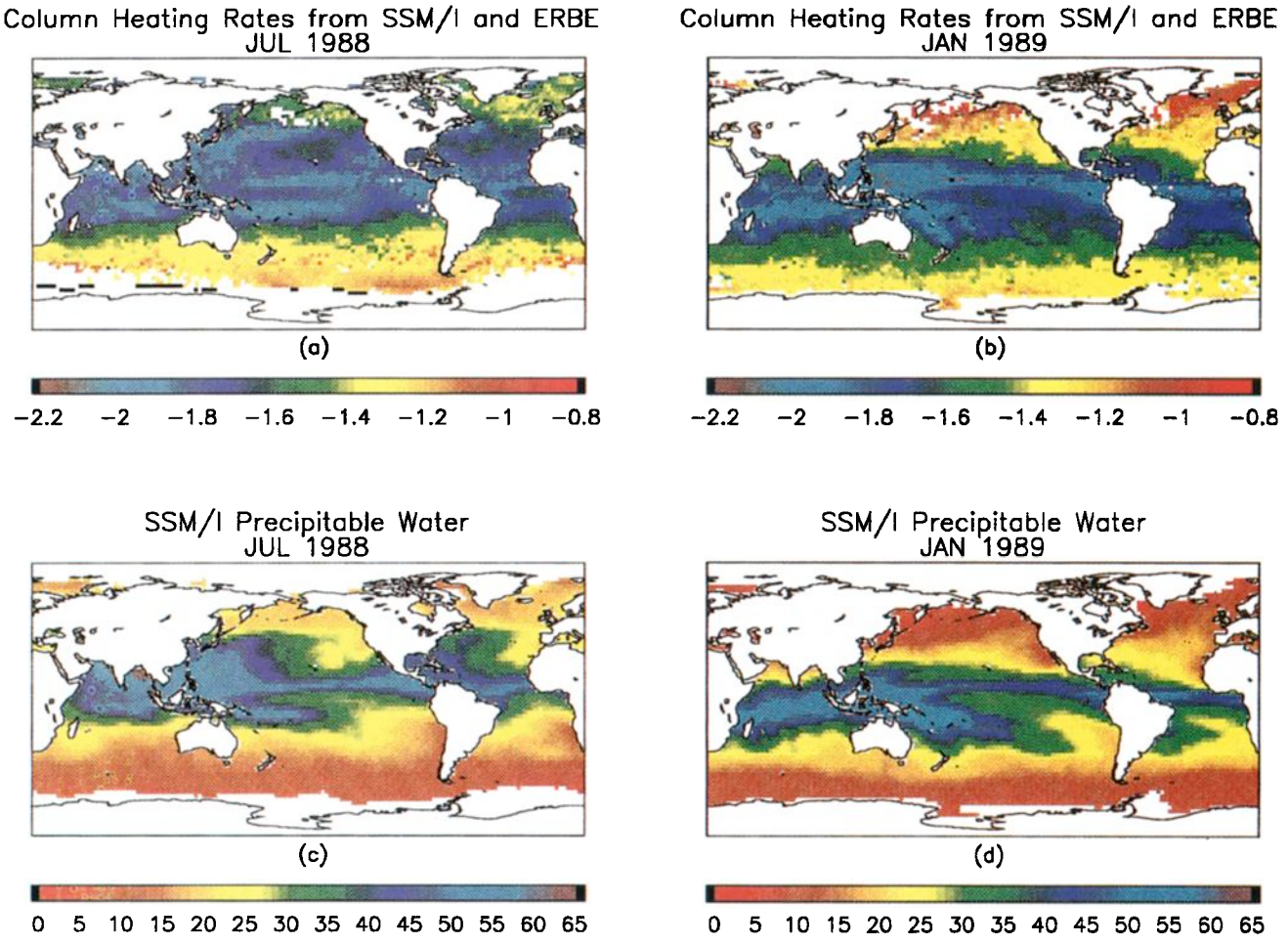


**Plate 2.** (a) and (b) Clear sky column cooling rate distributions for July 1988 and January 1989 (in units of K $d^{-1}$. (c) and (d) Same as Plates 2a and 2b except for vertically integrated water vapor (in units of kg $m^{-2}$).

### 6.2. Cloudy Sky Cooling Rate Differences

We introduce the effects of clouds on the column cooling rate in terms of the following difference quantity

$$\Delta\left(\frac{dT}{dt}\right) = \left(\frac{dT}{dt}\right)_{\text{cloudy}} - \left(\frac{dT}{dt}\right)_{\text{clear}},$$

which, in flux form, is

$$\Delta\left(\frac{dT}{dt}\right) = -\frac{gF_\infty}{c_p p_s}[\Delta F_g + \Delta F_\infty], \qquad (12)$$

where $\Delta F_g$ and $\Delta F_\infty$ are the respective differences between all (cloudy) sky and clear sky fluxes. Since the fluxes emitted to the surface under normal cloudy conditions exceed the clear sky fluxes, $\Delta F_g > 0$, so that this term contributes to the radiative cooling of the column. Conversely, since the radiating temperature of clouds is typically colder than the equivalent radiating temperature of the surrounding clear sky, $\Delta F_\infty < 0$, so the second term of (12) contributes to column heating. Therefore the net effect of clouds on the column longwave heating rate occurs as a result of the difference between two competing factors, a cooling factor associated with increased emission by clouds in the atmosphere to the surface and a heating factor associated with decreased emission by clouds in the atmosphere to space.

The flux difference quantity $\Delta F_\infty$ is available from ERBE analyses (this is the negative of the longwave cloud radiative forcing), whereas global estimates of $\Delta F_g$ is a function of unknown cloud base temperatures among other parameters. It is therefore not possible to estimate the global effect of clouds on the column heating rate using presently available measurements from satellites and this remains a topic of some challenge for future research. However, it is possible to provide upper and lower bounds on the effects of clouds on the column heating rate. One extreme, we propose, may be obtained simply by setting $\Delta F_g$ either to zero or more realistically, as we show below to a small, constant value $\delta_{\min}$. With $\delta_{\min} = 0$, we obtain the maximum possible heating potential of clouds and for convenience refer to this extreme as the heating limit. The other extreme occurs when $\Delta F_g$ is set to its maximum possible value which we propose occurs when the downwelling long-

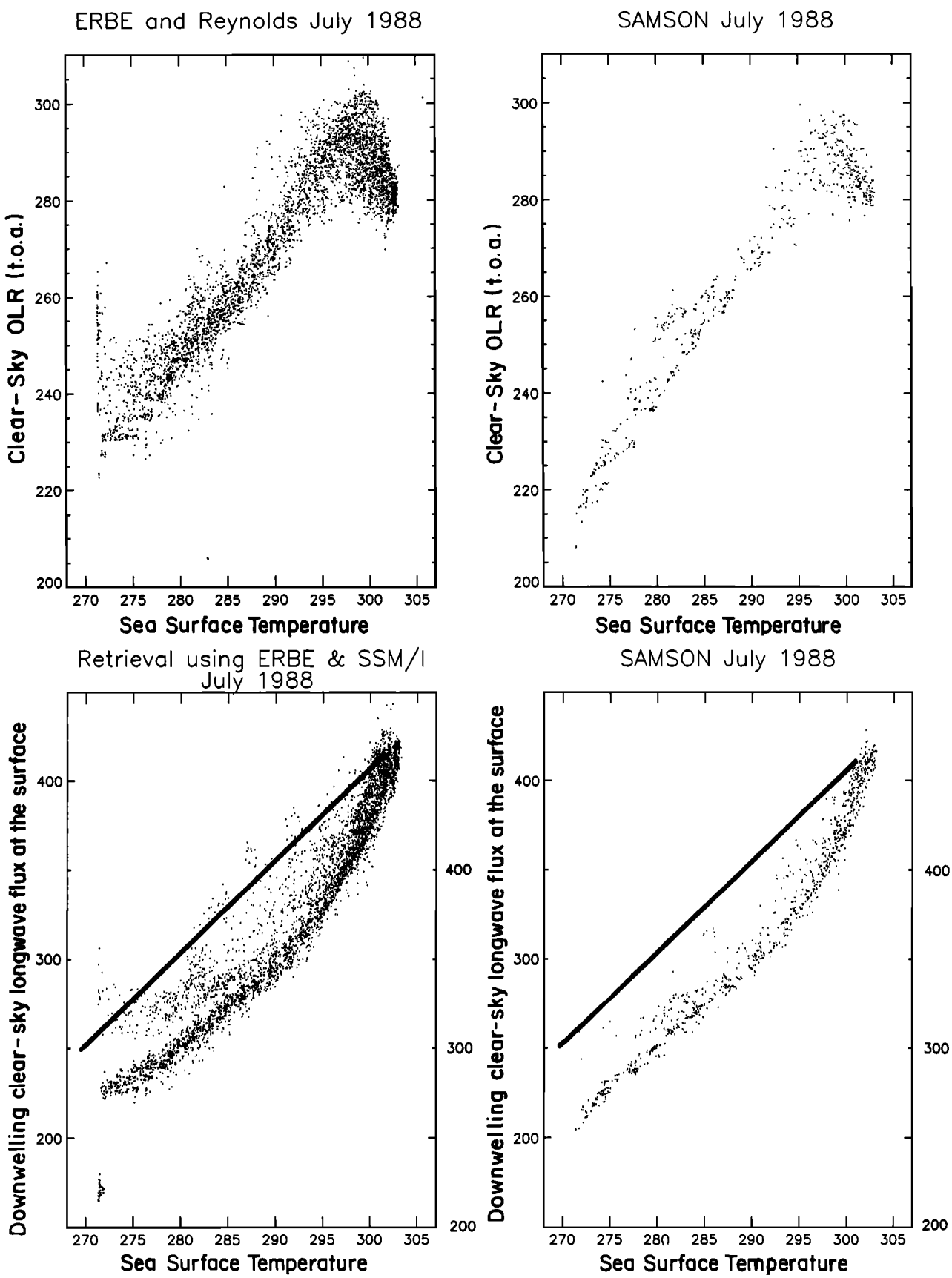


**Figure 7.** $F_\infty$ as a function of SST (top two panels) from ERBE (left) and SAMSON (right). $F_g$ as a function of SST (bottom panels) derived from the retrieval method described in the text (left) and from SAMSON (right). The solid line on each of the bottom panels represents blackbody emission at the prescribed value of the SST and the scale on the left represents the scale of this blackbody flux.

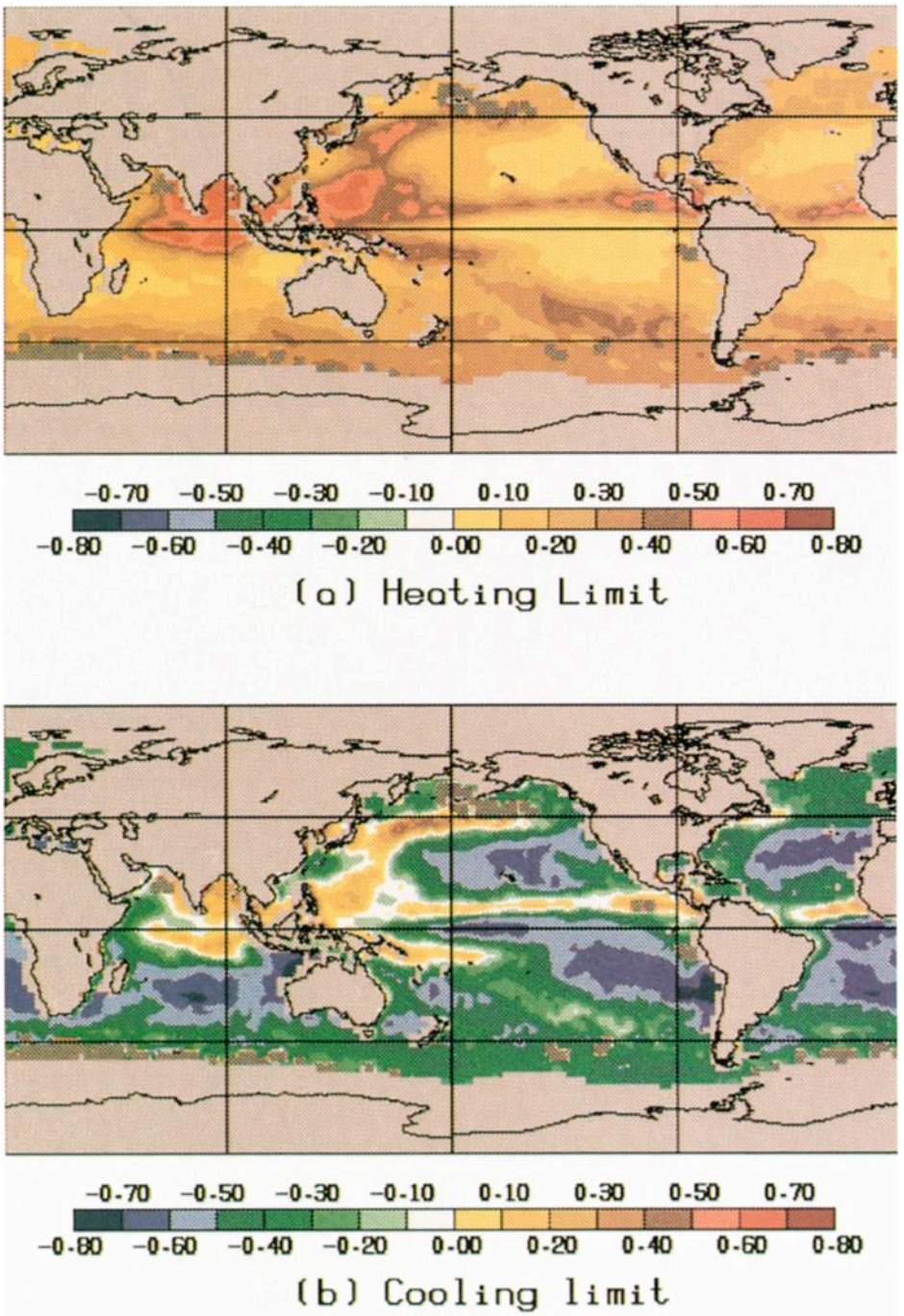


**Plate 3.** (a) The heating limit of clouds on the column radiative cooling rate and (b) the cooling limit defined assuming a cloud base temperature that is 2 K less than the SST. Both results are for July 1988.

wave flux to the surface under cloudy skies equals the blackbody flux emitted by the surface and specified by the given SST. For convenience, we represent this extreme by $\delta_{\max}$, and define it in terms of a small temperature difference $\Delta T$ according to

$$\delta_{\max}(\Delta T) = \sigma(T_s - \Delta T)^4 - (F_g)_{\text{clear}},$$

where $T_s$ is the given SST. Although the maximum cooling potential of clouds obviously occurs when $\Delta T = 0$, this clearly represents an extreme circumstance that occurs, for example, in the case of thick fog on the ground. We propose that a more realistic cooling limit is one that corresponds to a non–zero value of $\Delta T$ and we use $\Delta T = 2$ K for the example given below.

Distributions of the heating and cooling limits of clouds are presented in Plates 3*a* and 3*b*, respectively, for July 1988. The distribution shown for the heating limit (Plate 3*a*) is just the distribution of the longwave cloud forcing expressed here in heating rate units rather than in the more usual flux units. Regions of low clouds, such as over the eastern portions of the subtropical Pa-

cific and Atlantic Oceans, have a small impact on the heating, whereas regions of high, cold–top clouds, such as in the vicinity of the the Asian monsoon, the Pacific and Atlantic InterTropical Convergence Zones (ITCZs) and into the northern Pacific, dramatically contributes to this heating. A relevant highlight of the the cooling limit distribution (Plate 3*b*) is the large cooling associated with regions of low clouds and the persistence of column heating in regions of deep cloudiness.

### 6.3. Cloudy Sky Effects Relative to a Moisture Threshold

It is reasonable to propose that the effects of clouds on the infrared column cooling in certain regions can be more tightly defined than given by the bounds illustrated in Plates3*a* and 3*b*. For example, under conditions of marine boundary layer stratiform cloud we may be able to define $\Delta F_g$ with tolerable accuracy in a manner very similar to that given above where $\delta_{\max}$ was defined for $\Delta T = 2$. In fact, the cloud effect on the column cooling in these regions as shown in Plate 3*b*, is probably a reasonable estimate of the actual effect of these low–level clouds.

We also suggest that where there is a sufficient water vapor burden, introduced here in terms a threshold value of $w$, the difference between cloudy and clear sky longwave flux to the ground is sufficiently small that uncertainties in the value of this difference are also acceptably small within say 10 W m$^{-2}$. In these regions the impact of clouds on the column cooling rate will thus resemble the heating limit illustrated in Plate 3*a*. It thus remains to test this hypothesis and establish the appropriate threshold value of $w$.

Flux difference data derived from three different sources, all displayed in Figure 8 as a function of $w$, are used to test this idea. The curves drawn represent the relationships between $\Delta F_g$ obtained from model calculations, and the symbols are monthly mean flux differences obtained from analyses of the TOGA surface radiation budget and radiosonde data. The horizontal bars attached to these points indicate the range of variability of clear sky $w$ that occurred during the given month. The solid line is the relationship obtained using monthly mean flux differences derived from simulations using the CSU GCM and thus represent a variety of cloud altitude conditions (it is relevant to recall that the CSU GCM does not have partial cloudiness). The remaining two curves are a result of radiative transfer calculations assuming completely overcast conditions with an optically thick cloud layers located between 8–9 km and 1–2 km, respectively. These calculations were performed using the *Stackhouse and Stephens* [1991] model and the McClatchey et al. tropical atmosphere and, as above, $w$ was varied by multiplying the specific humidity at each level by a constant multiplicative factor.

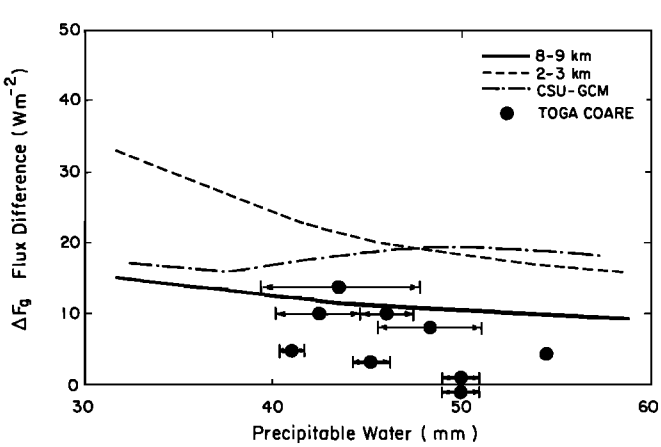


**Figure 8.** The difference between cloud sky and clear sky longwave flux to the surface as a function of the integrated water vapor content. Shown are flux differences derived from a radiative transfer model, the CSU GCM, and from the TOGA surface radiation budget data.

The largest flux differences occur when overcast low cloud conditions prevail. According to the results presented in Figure 8, we assume that the monthly mean value of $\Delta F_g$ for $w$ >30 kg m$^{-2}$ is 15 W m$^{-2}$ and that a reasonable measure of the uncertainty of this value is of the order of 10 W m$^{-2}$ based on the spread shown in Figure 8 and on the measured variances of the TOGA cloudy sky and clear sky longwave fluxes (Table 2b).

The July 1988 and January 1989 cloud heating difference distributions in regions where $w > 30$ kg m$^{-2}$ are presented in Plates 4*a* and 4*b*. This heating is largest in the western Pacific approaching a magnitude of 0.9 K d$^{-1}$ which, when contrasted against the results shown in Plates 2*a* and 2*b*, is approximately half of the clear sky column cooling in these regions. The net longwave radiative heating of the atmospheric column is then obtained as the sum of the heatings given in Plates 4*a* and 4*b* and the clear sky column cooling shown previously in Plates 2*a* and *b*. The combined heating distributions are presented in Plates 4*c* and 4*d* and these suggest the presence of a substantial longwave heating gradients stretching across the tropical Pacific south of the ITCZ in January (Plate 4*c*) and north of the ITCZ in July (Plate 4*d*). The eastern portions of the tropical Pacific are regions of prevalent low cloudiness and the net column cooling in these regions exceeds the clear sky values which are approximately 2 K d$^{-1}$. In contrast to this strong cooling in the eastern portions of the tropical and subtropical Pacific is the weaker cooling of approximately 1 K d$^{-1}$ in the western Pacific where heating by deep convective cloud systems (Plates 4*a* and 4*b*) approximately halve the clear sky values of the column cooling.

The longitudinal radiative heating gradients that are set up across the Pacific have the same sign as the gradients associated with latent heating due to precipitation. The significance of these heating gradients and the possible circulations they induce is studied by *Slingo and Slingo* [1989].

## 7. Summary and Conclusion

This paper is the final in a series of papers which seek to explore new uses of global satellite data to study rela-

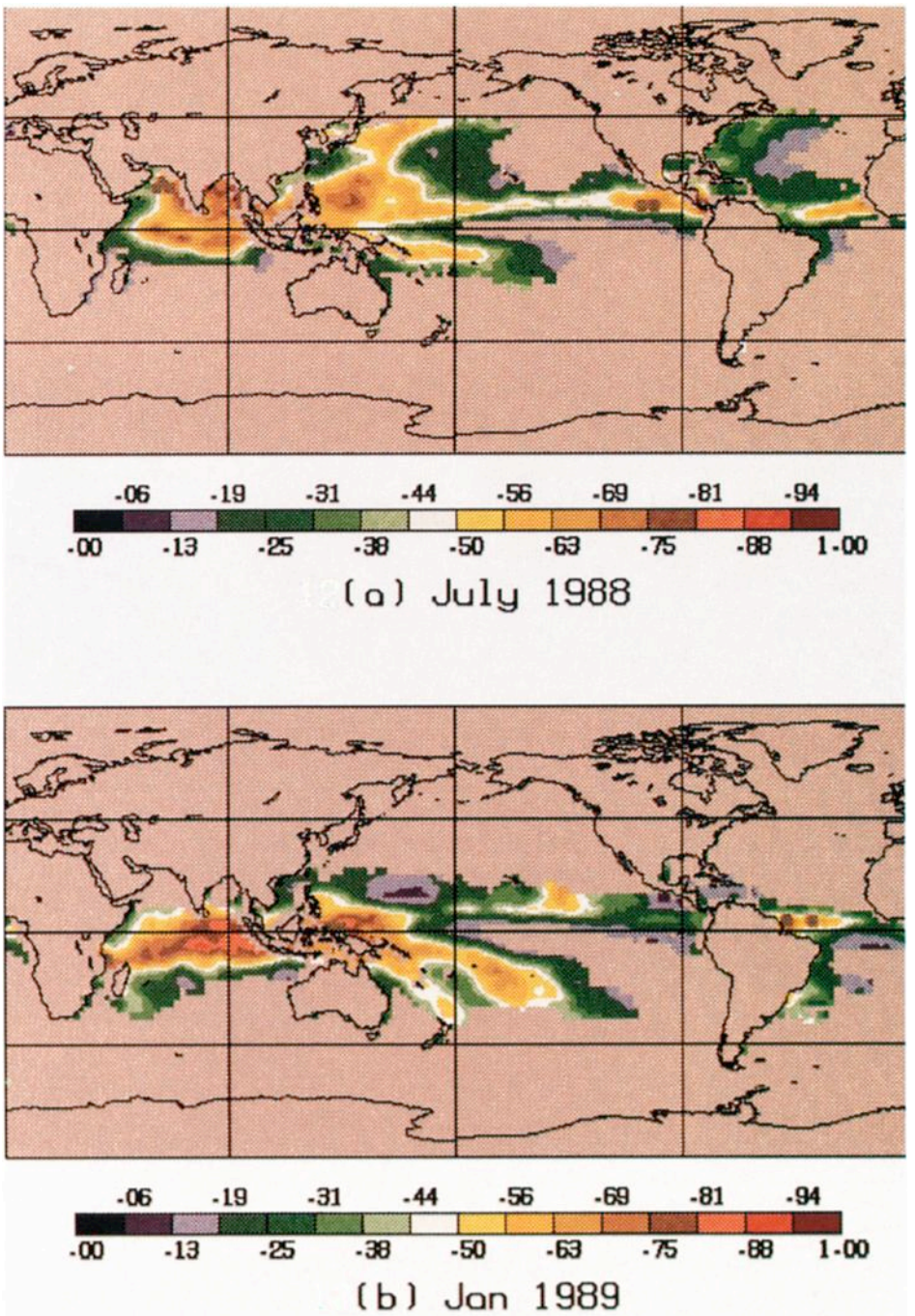


**Plate 4.** (a) and (b) The longwave column heating by clouds in an atmosphere for which $w > 30$ kg m$^{-2}$ derived assuming $\Delta F_g = 15$ W m$^{-2}$ for July 1988 and January 1989, respectively. (c) and (d) The net longwave column cooling (sum of Plates 2a and 2b and Plates 4a and 4b for July 1988 and January 1989, respectively, for those regions where $w > 30$ kg m$^{-2}$.

tionships between certain aspects of the energy budget of the climate system and its hydrological cycle. The motivation, in part, is to develop useful diagnostic tests of current global climate models. The present paper introduces a simple method for deriving climatological values of the longwave flux emitted from the clear sky atmosphere to the ground and presents a validation of this approach. A related goal of the research described in this paper is to apply these fluxes to the calculation of the column cooling rate of the atmosphere. We consider it appropriate to view this cooling as a fundamental measure of the activity of the Earth's greenhouse effect and the global character of this cooling in turn as an indirect measure of the Earth's hydrological cycle. As such, we explore bulk relationships between the clear sky column cooling rate and the hydrological cy-

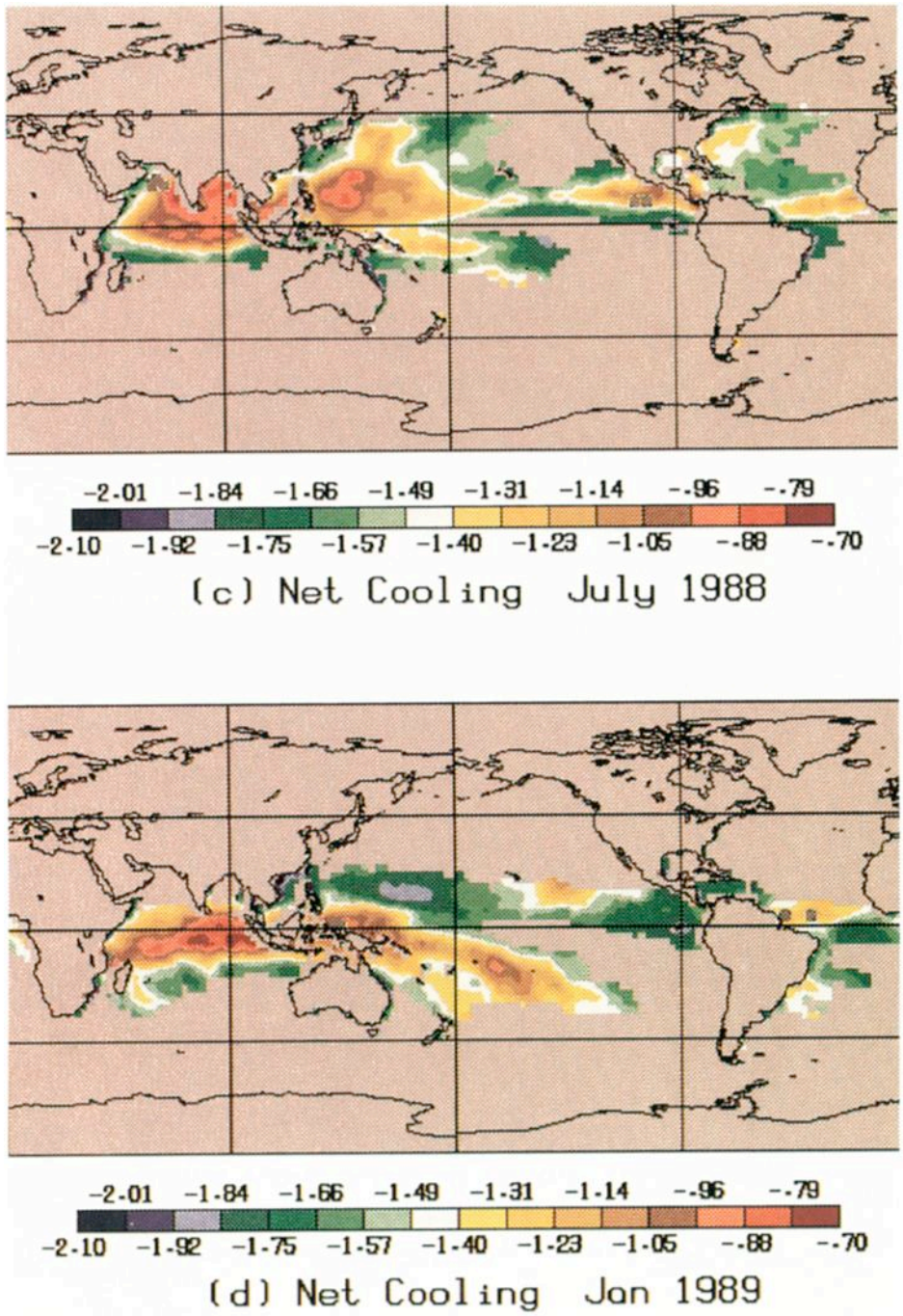


**Plate 4. (continued)**

cle as diagnosed by the column water vapor amount. We also explore, in a limited way and for specific regions, how we might assess the effects of clouds on this longwave cooling although it is clear that a more global assessment must await use of new satellite data that will allow us to estimate the contributions by clouds to the surface longwave fluxes and therefore to the column heating rates in a meaningful way.

The major results and conclusions of this study are as follows: 1. SAMSON simulations of the clear sky longwave fluxes to space and to the surface are employed in this study to assist in development of a retrieval of $F_g$. Simulations of the flux to space, $F_\infty$, as reported previously by *Slingo and Webb* [1992], generally match the ERBE estimates of the same fluxes within 5–10 W m$^{-2}$ with a small bias (of approximately 3 W m$^{-2}$) which also happens to be of a similar magnitude and sign of a reported bias in the ERBE clear sky flux data [*Harrison et al.*, 1988]. The uncertainty in the SAMSON clear sky monthly mean $F_g$ is also probably of the order of 10 W m$^{-2}$ although we have little data to confirm this uncertainty.

2. A new relationship between the ratio of $F_g$ and $F_\infty$ and the column water vapor $w$ is introduced. This relationship is derived over ocean surfaces that emit as an assumed blackbody. It is demonstrated using the SAM-

SON results how this ratio is approximately linear when $w > 20$ kg m$^{-2}$, as predicted by graybody radiative equilibrium arguments. When the water vapor amount is below 20 kg m$^{-2}$, the relationship, while still distinct, takes on a nonlinear curve of growth form. Independent surface longwave flux measurements, combined with $F_\infty$ simulated using measured radiosonde temperature and moisture profiles in a radiative transfer model, confirm the existence of this general flux ratio–$w$ relationship. The extent to which this relationship exists over land is not explored in this study, although it is likely that the relation will break down over surfaces of variable emissivity such as may occur over arid land regions.

3. A simple linear fit applied over the range $w > 20$ kg m$^{-2}$ was carried out to determine the slope and intercept coefficients. The values of these coefficients, together with SSM/I observations of $w$ and ERBE observations of the clear sky $F_\infty$, are used to obtain monthly mean values of $F_g$ over the oceans. Examples of the results of this simple retrieval are presented and contrasted with those from SAMSON and the rms difference between the retrieved and the simulated fluxes is $\pm 6$ W m$^{-2}$, which is considerably smaller than the uncertainty presently expected from the direct radiometric measurements of this flux.

4. We use our retrieval of $F_g$ from satellite measurements of $F_\infty$ and $w$ together with climatological values of surface pressure and SST to arrive at monthly mean distributions of the column-averaged clear sky longwave heating rates and propose that this heating rate has an uncertainty of approximately $\pm 0.2$ K d$^{-1}$. These column heating rates, when contrasted with the SSM/I fields of $w$ that were used to produce them, demonstrate a systematic increase (in cooling) as $w$ increases in an almost linear manner, as predicted by a simple analysis given in this paper. Under moist conditions, where $w > 40$ kg m$^{-2}$, the rate of growth of cooling with increasing $w$ slightly decreases due to a decreasing sensitivity of $F_\infty$ with increasing $w$. However, when viewed as a function of SST rather than as a function of $w$, the column cooling rate dramatically increases with increasing SST. This is shown to be due to the increase of emission from the atmosphere to the surface associated with increasing $w$ which is linked to the increasing SST. We deduce that this increase in the flux emitted from the atmosphere is more than twice the rate of increase of the flux emitted from the surface.

5. Upper and lower bounds on the effects of clouds on the column cooling rate of the atmosphere are established and, furthermore, we demonstrate how the longwave effects of clouds in a moist atmosphere where the column water vapor exceeds approximately 30 kg m$^{-2}$ may be estimated from presently available satellite data with an uncertainty estimated to be not significantly larger than 0.2 K d$^{-1}$. Based on the approach described in section 6, we show how clouds in these relatively moist regions decrease the column cooling by almost 50 % of the clear sky values and how we infer the presence of significant longitudinal gradients in column radiative heating across the equatorial and subtropical Pacific Ocean.

**Acknowledgments.** The principal author's research based on collecting and measuring surface radiation fluxes is supported by ONR contract N00014-91-J-422 P0002, and early aspects of this work were supported under NOAA grant NA90RAH0077, and together with PHD and LK by the U.S. Department of Energy under Contract DOE-FG02-89ER69027. PJM was supported by NOAA grant NA26GP0266 and by the NSF grant DPP-9113962 through subcontract 91–1178–01 with the North Carolina State University. Both AS and MW were supported under the U.K. Department of the Environment contract PECD 7/12/37, and the GCM research of DAR was supported under NASA grant NAG1-1266. While preparing this manuscript, the lead author was made aware of the research of V. Ramanathan dealing with topics similar to those discussed in this paper. The interested reader wishing to access the flux data collected as part of TOGA COARE and described in this paper can do so by using the e-mail address described further by *Cornwall et al.* [1993].

## References

Cess, R. D., E. G. Dutton, J. J. Deluisi, and F. Jiang, Determining surface solar absorption from broadband satellite measurements for clear skies: Comparison with surface measurements, *J. Clim.*, 4, 236–247, 1991.

Clough, S. A., F. X. Kneizys, L. S. Rothman, G. P. Anderson, and E. P. Shettle, Current issues in infrared atmospheric transparency, in *Atmospheric Transparency for Satellite Applications*, edited by G.V. Silvestini, CUEN, Capri, Italy, 1986.

Cornwall, C. R., C. L. Combs, J. M. Davis, G. L. Stephens, and S. K. Cox, CSU Radiation Budget pilot study for TOGA COARE, *CSU Atmos. Sci. Pap. 532*, 57 pp., Colo. State Univ., Fort Collins, 1993.

Dutton, E. G., An extended comparison between LOWTRAN7 computed and observed broadband thermal radiances: Global extreme and intermediate surface conditions, *J. Atmos. Oceanic Technol., 10*, 326–336, 1993.

Ellingson, R. G., J. Ellis, and S. Fels, The intercomparison of radiation codes in climate models: Longwave results, *J. Geophys. Res., 96*, 8929–8953, 1991.

Greenwald, T., G. L. Stephens, T. VonderHaar, and D. Jackson, A physical retrieval of cloud liquid water over the global oceans using SSM/I observations, *J. Geophys. Res., 98*, 18,471-18,488, 1993.

Gupta S., W. L. Darnell, and A. C. Wilber, A parameterization for longwave surface radiation from satellite data: Recent improvements, *J. Appl. Meteorol., 31*, 194–211, 1992.

Harrison, E. F., D. R. Brooks, P. Minnis, B. A. Wielicki, W. F. Staylor, G. G. Gibson, D. F. Young, F. M. Denn, and the ERBE Science Team, First estimates of the diurnal variation of longwave radiation from the multiple–satellite Earth Radiation Budget Experiment (ERBE), *Bull. Am. Meteorol. Soc., 69*, 1144–1151, 1988.

Hollinger, J., R. Lo, C. Poe, R. Savage, and J. Pierce, Special Sensor microwave/imager user's guide, *NRL Rep.*, Nav. Res. Lab.,
Washington, D. C., 1987.

House, F. B., A. Gruber, G. Hunt, and A. T. Mecherikunnel, History of satellite missions and measurements of the Earth Radiation Budget (1957–1984), *Rev. Geophys., 24*, 357–377, 1986.

Liu, W. T., T. Wang, and F. Wentz, Precipitable water and

surface humidity over the global oceans from SSM/I and ECMWF, *J. Geophys. Res.*, *97*, 2251–2264, 1992.

Manabe, S., and R. T. Wetherald, Thermal equilibrium of the atmosphere
with a given distribution of relative humidity, *J. Atmos. Sci.*,
*24*, 241–259, 1967.

McClatchey, R. A., R. W. Fenn, J. C. Selby, F. E. Volz and J. S. Goring, *Optical Properties of the Atmosphere*, 3rd ed., 107 pp., Air Force Cambridge Res. Labs, 1972.

Minnett, P. J., Surface oceanographic and atmospheric measurements made during the Mediterranean Aircraft–Ship Transmission Experiment (MASTEX) from the R/V *Alliance, SACLANT Cent. Memo., SM-264*, 131 pp. SACLANT Undersea Res. Cent., La Spezia, Italy, 1992.

Minnett, P. J., Measurement for satellite validation made from the RV Alliance during October and November 1991, *SACLANT Cent. Memo., SM-273*, 268 pp. SACLANT Undersea Research Centre, La Spezia, Italy, 1993.

NEWATER Steering Committee and Principal Investigators,
Collaborative research on the Northeast Water Polynya: Initial results from the 1992 *polar sea* cruise, *ES Trans. AGU., 74*, 185 and 195-196, 1993.

Pinker, R. T., and I. Laszlo, Modeling surface solar irradiance for satellite applications on a global scale, *J. Appl. Meteorol.*, *31*, 194–211, 1992.

Ramanathan, V., B. R. Barkstrom, and E. F. Harrison, Climate and the Earth's Radiation Budget, *Phys. Today*, 22–32, 1989.

Randall, D.A., et al., Intercomparison and interpretation of surface energy fluxes in atmospheric general circulation models, *J. Geophys. Res.*, *97*, 3711–3724, 1992.

Reynolds, R. W., A real–time global sea surface temperature analysis,
*J. Clim.*, *1*, 75–86, 1988.

Rodgers, C. D., The use of emissivity in atmospheric radiation calculations, *Q. J. R. Meteorol. Soc.*, *93*, 43–54, 1967.

Sabatini, R. R., and V. E Suomi, On the possibility of atmospheric infrared cooling estimates from satellite observations, *J. Atmos Sci.*, *19*, 349-350, 1962.

Schmetz, J., Towards a surface radiation climatology: Retrieval of downward irradiance from satellites , *Atmos. Res.*, *23*, 287-321, 1989.

Shine, K. P., On the cause of the relative greenhouse strength of gases such as halocarbons, *J. Atmos. Sci.*, *48*, 1513–1518, 1991.

Shine, K. P., and A. Sinha, Sensitivity of the Earth's climate to height dependent changes in the water vapor mixing ratio, *Nature*, *354*, 382–384, 1991.

Slingo, A., and J. M. Slingo, The response of a general circulation model to cloud longwave radiative forcing, I, Introduction and initial experiments, *Q. J. R. Meteorol. Soc.*, *114*, 1027–1062, 1989.

Slingo, A., and M. J. Webb, Simulation of clear sky outgoing longwave radiation over the oceans using operational analyses, *Q. J. R. Meteorol. Soc.*, *118*, 1117–1144, 1992.

Stackhouse, P. W., Jr., and G. L. Stephens, A theoretical and observational study of the radiative properties of cirrus: Results from FIRE 1986, *J. Atmos. Sci.*, *48*, 2044-2059, 1991.

Stephens, G.L., On the relationship between water vapour over the oceans and sea surface temperature. *J. Clim.*, *3*, 634-645, 1990.

Stephens, G. L., and T. J. Greenwald, Observations of the Earth's Radiation Budget in Relation to Atmospheric Hydrology, 1, Clear sky greenhouse effect and water vapor feedback, *J. Geophys.Res.*, *96*, 15,311-15,324, 1991a.

Stephens, G. L., and T. J. Greenwald, Observations of the Earth's Radiation Budget in relation to atmospheric hydrology, 2, Cloud effects and cloud feedback, *J. Geophys. Res.*, *96*, 15,325-15,340, 1991b.

Stephens, G. L., D. A. Randall, I. L. Wittmeyer, and D.A. Dazlich, Observations of the Earth's Radiation Budget in relation to atmospheric hydrology, 3, Comparison of observations over oceans with a GCM, *J. Geophys. Res.*, *98*, 4931-4950, 1993.

Stephens, G.L., D.L. Jackson and J.J Bates, A comparison of SSM/I and TOVS column water vapor data over global oceans, *Meteorol. Atmos. Phys.*, in press, 1994.

Webb, M.J., A. Slingo, and G.L. Stephens, Seasonal variations of the clear sky greenhouse effect: The role of changes in atmospheric temperatures and humidities, *Clim. Dyn.*, *9*, 117–129, 1993.

**P.H. Daum and L. Kleinman, Environmental Chemistry Division, Brookhaven National Laboratory, Upton, NY 11973-5000.**

**P.J. Minnett, Oceanographic and Atmospheric Sciences Division, Brookhaven National Laboratory, Upton, NY 11973-5000.**

**D.A. Randall, G.L. Stephens, and I. Wittmeyer, Department of Atmospheric Sciences, Colorado State University, Fort Collins, CO 80523.**

**A. Slingo and M.J. Webb, Hadley Center for Climate Prediction and Research, Meteorological Office, Bracknell, England.**

(Received November 8, 1993; revised April 6, 1994; accepted April 20, 1994.)